2013

Lattice Boltzmann Simulations of Thermal Convective Flows in Two Dimensions

Jia Wang

Donghai Wang

Pierre Lallemand

Li-Shi Luo
Old Dominion University, lluo@odu.edu

Original Publication Citation

Wang, J., Wang, D. H., Lallemand, P., & Luo, L. S. (2013). Lattice Boltzmann simulations of thermal convective flows in two dimensions. *Computers and Mathematics with Applications, 65*(2), 262-286. doi:10.1016/j.camwa.2012.07.001

Computers and Mathematics with Applications 65 (2013) 262–286

Contents lists available at SciVerse ScienceDirect

Computers and Mathematics with Applications

journal homepage: www.elsevier.com/locate/camwa

Lattice Boltzmann simulations of thermal convective flows in two dimensions

Jia Wang [a], Donghai Wang [a], Pierre Lallemand [b], Li-Shi Luo [c,b,*]

[a] State Key Laboratory of Severe Weather, Chinese Academy of Meteorological Sciences, Beijing 100081, China

[b] Beijing Computational Science Research Center, Beijing, 100084, China

[c] Department of Mathematics & Statistics and Center for Computational Sciences, Old Dominion University, Norfolk, VA 23529, USA

ARTICLE INFO

Keywords:
MRT lattice Boltzmann model for thermo-hydrodynamics in 2D
Square cavity with differentially heated vertical walls
Rayleigh–Bénard convection
Boundary conditions for thermal flows

ABSTRACT

In this paper we study the lattice Boltzmann equation (LBE) with multiple-relaxation-time (MRT) collision model for incompressible thermo-hydrodynamics with the Boussinesq approximation. We use the MRT thermal LBE (TLBE) to simulate the following two flows in two dimensions: the square cavity with differentially heated vertical walls and the Rayleigh–Bénard convection in a rectangle heated from below. For the square cavity, the flow parameters in this study are the Rayleigh number $\mathrm{Ra} = 10^3$–10^6, and the Prandtl number $\mathrm{Pr} = 0.71$; and for the Rayleigh–Bénard convection in a rectangle, $\mathrm{Ra} = 2 \cdot 10^3$, 10^4 and $5 \cdot 10^4$, and $\mathrm{Pr} = 0.71$ and 7.0.

1. Introduction

The lattice Boltzmann (LB) modeling of thermo-hydrodynamic flows has been an active area of research since the creation of the lattice Boltzmann equation (LBE) (cf., e.g., reviews [1,2] and references therein). The initial effort of thermo-LBE (TLBE) was focused on the energy-conserving LB models [3–7]. However, the energy-conserving LB models suffer severe numerical instability [6], which is due to spurious coupling in the energy-conserving LB models and cannot be completely removed [8].

To overcome the numerical instability inherent to the energy-conserving TLBE models [8], the approach to treat the temperature as a passive scalar was proposed [9]. In this approach the temperature is independently modeled by an advection–diffusion equation which is equivalent to the Boussinesq approximation valid for incompressible flows. The passive-scalar TLBE uses two sets of distribution functions—one for mass and momentum and the other for temperature. Similar to the LBE for only the mass and momentum conservations [10,11], the passive-scalar TLBE can be directly derived from the continuous Boltzmann equation [12–14]. A slightly different approach of passive-scalar TLBE is the hybrid approach which solves the temperature equation by finite difference scheme [8,15]. We note that most previous TLBE schemes [9,12–14] are based on the lattice Bhatnagar–Gross–Krook (BGK) model with one relaxation time which tunes *all* transport coefficients and higher-order dissipation in the LBE [16,8]. The single-relaxation-time (SRT) collision model directly results in two inherent defects of the lattice BGK (LBGK) model: its numerical instability and inaccurate boundary conditions [16,17,8,18].

The passive-scalar TLBE used in this work is based on the framework of the LBE with multiple-relaxation-time (MRT) model due to d'Humières [19] and the LB model for the advection–diffusion equation due to Ginzburg [20–23] and Ginzburg

* Corresponding author at: Department of Mathematics & Statistics and Center for Computational Sciences, Old Dominion University, Norfolk, VA 23529, USA. Tel.: +1 757 683 5295.

E-mail address: lluo@odu.edu (L.-S. Luo).

0898-1221/$ – see front matter
doi:10.1016/j.camwa.2012.07.001

and d'Humières [24]. It has been unequivocally demonstrated that the MRT-LB models are superior over their LBGK counterparts in terms of accuracy, numerical stability, and computational efficiency [16,17,8,18]. In addition, the MRT formalism is imperative to accurately treat boundary conditions in the LBE simulations [25,17,26,18] and inaccuracy of boundary conditions is one of the most severe defects inherent to the LBGK model [27,17,1,28,18].

To demonstrate the efficacy of the MRT-TLBE scheme, we will simulate the two following thermal flows in two dimensions. The first one is the square cavity with differentially heated vertical walls; and the parameters for this flow are the Rayleigh number $\mathrm{Ra} = 10^3$–10^6 and the Prandtl number $\mathrm{Pr} = 0.71$. The second one is the Rayleigh–Bénard convection in a rectangle heated from below and subject to gravity; and the flow parameters are $\mathrm{Ra} = 2 \cdot 10^3$, 10^4 and $5 \cdot 10^4$, and $\mathrm{Pr} = 0.71$ and 7.0. Both these flows have been studied previously. In this paper we intend to systematically investigate the convergence behavior, the effect of the Mach number and the influence of different boundary conditions, and the computational speed of the MRT-TLBE. We also intend to provide benchmark quality results which can be compared with the existing data.

The remainder of this paper is organized as follows. Section 2 succinctly describes the MRT-TLBE scheme in two-dimensions, its boundary conditions, as well as its implementations. Sections 3 and 4 present the numerical results for the square cavity with differentially heated vertical walls and the Rayleigh–Bénard convection in a rectangle heated from below, respectively. Finally, Section 5 concludes the paper.

2. MRT-LB model

We consider the lattice Boltzmann (LB) model for thermal fluids in two dimensions (2D). The discrete velocity set is that of D2Q9 model:

$$\boldsymbol{c}_i = \begin{cases} (0,0), & i = 0, \\ (1,0)c,\ (0,1)c,\ (-1,0)c,\ (0,-1)c, & i = 1\text{–}4, \\ (1,1)c,\ (-1,1)c,\ (-1,-1)c,\ (1,-1)c, & i = 5\text{–}8, \end{cases} \tag{1}$$

where $c := \delta x/\delta t$, and δx and δt are the lattice spacing and discrete time step size, respectively. The thermo-LB (TLB) model consists of two sets evolution equations: one for the mass and momentum conservation, and the other for the temperature.

The evolution equation for the mass and momentum conservations can be succinctly written as the following:

$$\mathbf{f}(\boldsymbol{x}_j + \boldsymbol{c}\delta t, t_n + \delta t) = \mathbf{f}(\boldsymbol{x}_j, t_n) + \mathbf{Q}(\boldsymbol{x}_j, t_n) + \mathbf{F}(\boldsymbol{x}_j, t_n), \tag{2a}$$

$$\mathbf{Q} = -\mathsf{M}^{-1} \cdot \mathsf{S} \cdot \left[\mathbf{m}(\boldsymbol{x}_j, t_n) - \mathbf{m}^{(\mathrm{eq})}(\boldsymbol{x}_j, t_n)\right], \tag{2b}$$

where the following convenient notations have been used:

$$\mathbf{f}(\boldsymbol{x}_j, t_n) := (f_0(\boldsymbol{x}_j, t_n), f_1(\boldsymbol{x}_j, t_n), \ldots, f_8(\boldsymbol{x}_j, t_n))^{\dagger},$$

$$\mathbf{f}(\boldsymbol{x}_j + \boldsymbol{c}\delta t, t_n + \delta t) := (f_0(\boldsymbol{x}_j, t_n + \delta t), f_1(\boldsymbol{x}_j + \boldsymbol{c}_1\delta t, t_n + \delta t), \ldots, f_8(\boldsymbol{x}_j + \boldsymbol{c}_8\delta t, t_n + \delta t))^{\dagger},$$

$$\mathbf{m}(\boldsymbol{x}_j, t_n) := (m_0(\boldsymbol{x}_j, t_n), m_1(\boldsymbol{x}_j, t_n), \ldots, m_8(\boldsymbol{x}_j, t_n))^{\dagger},$$

$$\mathbf{m}^{(\mathrm{eq})}(\boldsymbol{x}_j, t_n) := (m_0^{(\mathrm{eq})}(\boldsymbol{x}_j, t_n), m_1^{(\mathrm{eq})}(\boldsymbol{x}_j, t_n), \ldots, m_8^{(\mathrm{eq})}(\boldsymbol{x}_j, t_n))^{\dagger},$$

$$\mathbf{F} := (0, F_1, F_2, \ldots, F_8)^{\dagger},$$

in which † denotes transpose, f_i is the distribution function corresponding to $\boldsymbol{c}_i$, m_i and $m_i^{(\mathrm{eq})}$ are (velocity) moments and their equilibrium functions, respectively, and F_i is the component of the forcing projected to the direction of $\boldsymbol{c}_i$. The forcing term $\mathbf{F}$ in the LBE (2a) is implemented by using a splitting scheme [8,29], of which the details will be described later in Section 2.2.

The transformation matrix M transforms the distributions $\{f_i\}$ to their (velocity) moments $\{m_i\}$. To determine the transformation matrix M, the ordering of the moments must be prescribed first. The ordering of the moments we use here is:

$$\begin{aligned} \mathbf{m} &= (m_0, m_1, m_2, m_3, m_4, m_5, m_6, m_7, m_8)^{\dagger} \\ &= (\rho, j_x, j_y, e, p_{xx}, p_{xy}, q_x, q_y, \varepsilon)^{\dagger}, \end{aligned} \tag{3}$$

where ρ is the mass density, $\boldsymbol{j} := (j_x, j_y) = \rho(u, v) := \rho\boldsymbol{u}$ is the flow momentum and $\boldsymbol{u}$ is flow velocity, e, p_{xx} and p_{xy} are the second-order moments corresponding to energy and two off-diagonal components of the stress tensor, respectively, q_x and q_y are the third-order moments corresponding to x and y components of the energy flux, respectively, and ε is the fourth-order moment of energy square. With the ordering of the moments specified as the above, the transform matrix can be easily constructed:

$$\mathsf{M} = \begin{pmatrix} 1 & 1 & 1 & 1 & 1 & 1 & 1 & 1 & 1 \\ 0 & 1 & 0 & -1 & 0 & 1 & -1 & -1 & 1 \\ 0 & 0 & 1 & 0 & -1 & 1 & 1 & -1 & -1 \\ -4 & -1 & -1 & -1 & -1 & 2 & 2 & 2 & 2 \\ 0 & 1 & -1 & 1 & -1 & 0 & 0 & 0 & 0 \\ 0 & 0 & 0 & 0 & 0 & 1 & -1 & 1 & -1 \\ 0 & -2 & 0 & 2 & 0 & 1 & -1 & -1 & 1 \\ 0 & 0 & -2 & 0 & 2 & 1 & 1 & -1 & -1 \\ 4 & -2 & -2 & -2 & -2 & 1 & 1 & 1 & 1 \end{pmatrix}. \tag{4}$$

Note that the product of M and its transpose $\mathsf{M}^\dagger$, $\mathsf{M}\cdot\mathsf{M}^\dagger$, is a diagonal matrix, thus M^{-1} can be trivially obtained. The elements of the second and third rows of M correspond to the x and y components $\{\boldsymbol{c}_i\}$, respectively, it thus uniquely determines the ordering of the discrete velocity set $\{\boldsymbol{c}_i\}$.

There are three conserved quantities in this model: the mass density ρ and the two components of the momentum $\boldsymbol{j} = \rho\boldsymbol{u}$. Since we are only interested in incompressible fluids in this work, we will use the following approximations:

$$\rho = \rho_0 + \delta\rho, \quad \rho_0 = 1, \delta\rho = \sum_{i=0}^{8} f_i, \tag{5a}$$

$$\boldsymbol{j} = \rho_0\boldsymbol{u} = \rho_0(u, v), \quad \rho_0\boldsymbol{u} = \sum_{i=0}^{8} \boldsymbol{c}_i f_i. \tag{5b}$$

That is, we shall only consider fluctuations of ρ and $\boldsymbol{u}$ about $\rho_0 = 1$ and $\boldsymbol{u} = \boldsymbol{0}$, respectively. This helps to significantly reduce round-off errors in simulations, especially with single-precision arithmetic on graphic processing units (GPUs). Accordingly, the equilibrium moments are then defined as:

$$m_3^{(\text{eq})} = -2\delta\rho + 3\rho_0\boldsymbol{u}\cdot\boldsymbol{u}, \tag{6a}$$

$$m_4^{(\text{eq})} = \rho_0(u^2 - v^2), \qquad m_5^{(\text{eq})} = \rho_0 uv \tag{6b}$$

$$m_6^{(\text{eq})} = -\rho_0 u, \qquad m_7^{(\text{eq})} = -\rho_0 v, \tag{6c}$$

$$m_8^{(\text{eq})} = \delta\rho - 3\rho_0\boldsymbol{u}\cdot\boldsymbol{u}. \tag{6d}$$

Note that the equilibria of the conserved moments are themselves, thus $m_0^{(\text{eq})} = \delta\rho$, $m_1^{(\text{eq})} = \rho_0 u$, and $m_2^{(\text{eq})} = \rho_0 v$. With the above choice of the equilibria, the speed of sound waves in the unit of $c := \delta x/\delta t = 1$ is

$$c_s = \frac{1}{\sqrt{3}}. \tag{7}$$

With the ordering of $\{m_i\}$ given in Eqs. (3), the diagonal relaxation matrix is given by:

$$\mathsf{S} = \text{diag}(0, 1, 1, s_e, s_\nu, s_\nu, s_q, s_q, s_\varepsilon), \tag{8}$$

where $s_i \in (0, 2)$ for non-conserved modes, and specifically [30,26],

$$s_\nu = \frac{2}{6\nu + 1}, \qquad s_q = 8\frac{(2 - s_\nu)}{(8 - s_\nu)}. \tag{9}$$

The shear viscosity ν and bulk viscosity ζ in the model are

$$\nu = \frac{1}{3}\left(\frac{1}{s_\nu} - \frac{1}{2}\right), \qquad \zeta = \frac{1}{3}\left(\frac{1}{s_e} - \frac{1}{2}\right). \tag{10}$$

Unless stated otherwise, we will use $s_e = s_\varepsilon = s_\nu$, *i.e.*, the two-relaxation-time (TRT) model [20,31,32].

The temperature T is modeled by the following evolution equation

$$g(\boldsymbol{x}_j + \boldsymbol{c}\delta t, t_n + \delta t) = g(\boldsymbol{x}_j, t_n) - \mathsf{N}^{-1}\cdot\mathsf{Q}\cdot\left[\mathbf{n}(\boldsymbol{x}_j, t_n) - \mathbf{n}^{(\text{eq})}(\boldsymbol{x}_j, t_n)\right], \tag{11}$$

where the notations are similar to the evolution Eq. (2) for $\{f_i\}$, but with only five discrete velocities: $\{\boldsymbol{c}_i | i = 0, 1, \ldots, 4\}$ and corresponding distribution functions $\{g_i | i = 0, 1, \ldots, 4\}$. The transformation matrix N is given by

$$\mathsf{N} = \begin{pmatrix} 1 & 1 & 1 & 1 & 1 \\ 0 & 1 & 0 & -1 & 0 \\ 0 & 0 & 1 & 0 & -1 \\ -4 & 1 & 1 & 1 & 1 \\ 0 & 1 & -1 & 1 & -1 \end{pmatrix}. \tag{12}$$

The temperature T is the only conserved quantity in the system of $\{g_i\}$ and is computed by

$$T = \sum_{i=0}^{4} g_i. \tag{13}$$

The equilibrium moments $\{n_i^{(eq)} | i = 0, 1, \ldots, 4\}$ corresponding to $\{g_i | i = 0, 1, \ldots, 4\}$ are

$$n_0^{(eq)} = T, \qquad n_1^{(eq)} = uT, \qquad n_2^{(eq)} = vT, \qquad n_3^{(eq)} = aT, \qquad n_4^{(eq)} = 0, \tag{14}$$

where the velocity field $(u, v) = \boldsymbol{u}$ is obtained from the evolution Eq. (2) of $\{f_i\}$ and a is a constant to be determined later.

The diagonal relaxation matrix Q in Eq. (11) is given by

$$\mathsf{Q} = \mathrm{diag}(0, \sigma_\kappa, \sigma_\kappa, \sigma_e, \sigma_\nu). \tag{15}$$

The relaxation rate σ_κ determines the heat diffusivity κ:

$$\kappa = \frac{(4+a)}{10}\left(\frac{1}{\sigma_\kappa} - \frac{1}{2}\right). \tag{16}$$

To attain the isotropy for the fourth-order (error) term resulting from Eq. (11), σ_κ and σ_ν must satisfy the following relationship similar to Eq. (9) between s_q and s_ν:

$$\left(\frac{1}{\sigma_\nu} - \frac{1}{2}\right)\left(\frac{1}{\sigma_\kappa} - \frac{1}{2}\right) = \frac{1}{6}. \tag{17}$$

In addition, there exists a relationship between σ_e and σ_κ. If we fix σ_κ as

$$\frac{1}{\sigma_\kappa} - \frac{1}{2} = \frac{\sqrt{3}}{6}, \tag{18}$$

then additional constraints can be obtained:

$$\frac{1}{\sigma_e} - \frac{1}{2} = \frac{1}{\sigma_\nu} - \frac{1}{2} = \frac{\sqrt{3}}{3}. \tag{19}$$

The above values of σ_e and σ_ν will be used throughout the present work. The stability of the D2D5 model has been studied by Ginzburg et al. [33,34] and Ginzburg [35]. To avoid "checkerboard" type instability along the diagonal directions $(\pm 1, \pm 1)$, we must maintain $a < 1$. This limits the value of κ and thus one has to release previous conditions on the relaxation rates to simulate low Prandtl number fluids. With the above choice of σ_κ, the thermal diffusivity κ is given by

$$\kappa = \frac{\sqrt{3}\,(4+a)}{60}. \tag{20}$$

2.1. Macroscopic equations

In this work, we will study the 2D Rayleigh–Bénard (RB) convection of fluids in a rectangular box which is driven by buoyancy effect in the vertical direction. As usual, fluids are assumed to be incompressible thus the pressure influence on the density variation is neglected. The density variation due to temperature T is approximated by the following linear relationship

$$\rho = \rho_0[1 + \alpha(T - T_0)], \qquad \alpha := \frac{1}{\rho_0}\frac{\partial \rho}{\partial T}\bigg|_p, \tag{21}$$

where ρ_0 and T_0 are reference density and temperature, respectively, and α is the thermal expansion coefficient. Furthermore, the transport coefficients in the system, *i.e.*, the shear viscosity ν and the thermal diffusivity κ, and the thermal expansion coefficient α are treated as constants. Consequently we only consider the effect of density difference in the buoyancy term, and neglect the viscous heat dissipation and compression work due to the pressure, that is, the Boussinesq approximation.

In the thermal lattice Boltzmann equation described in the previous section, the temperature T is treated as a passive scalar which is transported by the velocity field but does not affect the velocity field except through the buoyancy force. Thus, the macroscopic equations derived from the TLBE are:

$$\partial_t \boldsymbol{u} + \boldsymbol{u}\cdot\nabla\boldsymbol{u} = -\frac{1}{\rho_0}\nabla p + \nu\nabla^2\boldsymbol{u} + \alpha(T - T_0)\boldsymbol{g}, \tag{22a}$$

$$\nabla\cdot\boldsymbol{u} = 0, \tag{22b}$$

$$\partial_t T + \boldsymbol{u}\cdot\nabla T = \kappa\nabla^2 T. \tag{22c}$$

In the coordinate system we use, the buoyancy force is given by

$$\boldsymbol{F} = \rho_0\alpha(T - T_0)\boldsymbol{g} = -\rho_0\alpha(T - T_0)g\hat{\boldsymbol{y}}, \tag{23}$$

where g is the gravity, $g = 9.81\ (\mathrm{m\,s^{-2}})$, and $\hat{\boldsymbol{y}}$ is the unit vector in vertical direction or y axis. Thus the projection of the force $\boldsymbol{F}$ onto the velocity space, F_i, in Eq. (2a) is given by Luo [36]:

$$F_i = -3w_i\frac{\boldsymbol{c}_i \cdot \boldsymbol{F}}{c^2} = 3w_i\rho_0\alpha(T - T_0)g\frac{\boldsymbol{c}_i \cdot \hat{\boldsymbol{y}}}{c^2}, \tag{24}$$

where $w_0 = 0$, $w_{1,2,3,4} = 1/9$ and $w_{5,6,7,8} = 1/36$.

Two dimensionless numbers characterize the system of thermo-hydrodynamic equations (2): the Prandtl number, Pr, and the Rayleigh number, Ra, which are defined as

$$\mathrm{Pr} = \frac{\nu}{\kappa}, \qquad \mathrm{Ra} = \mathrm{Gr}\cdot\mathrm{Pr}, \qquad \mathrm{Gr} = \frac{\alpha g\Delta TL^3}{\nu^2}, \tag{25}$$

where Gr is the Grashof number, and ΔT and L are the characteristic temperature and length in the system, respectively. With the following scalings,

$$\boldsymbol{x} \to \frac{\boldsymbol{x}}{L}, \qquad t \to \frac{t\kappa}{L^2}, \qquad \boldsymbol{u} \to \frac{\boldsymbol{u}L}{\kappa}, \qquad p \to \frac{pL^2}{\rho_0\kappa^2}, \qquad \theta := \frac{(T - T_0)}{\Delta T}$$

the thermo-hydrodynamic equations (2) can be written in dimensionless form,

$$\partial_t\boldsymbol{u} + \boldsymbol{u}\cdot\nabla\boldsymbol{u} = -\nabla p + \mathrm{Pr}\,\nabla^2\boldsymbol{u} + \mathrm{Ra}\,\mathrm{Pr}\,\theta\hat{\boldsymbol{g}}, \tag{26a}$$

$$\nabla\cdot\boldsymbol{u} = 0, \tag{26b}$$

$$\partial_t\theta + \boldsymbol{u}\cdot\nabla\theta = \nabla^2\theta, \tag{26c}$$

where $\hat{\boldsymbol{g}}$ is unit vector in the direction of the gravitation. The speed of sound c_s has to be rescaled, *i.e.*, $c_s \to c_sL/\kappa$. However, the Mach number Ma remains the same.

The shear viscosity ν and thermal diffusivity κ are determined in terms of Pr and Ra and other parameters in simulations:

$$\nu = \sqrt{\frac{\mathrm{Pr}\,\alpha g\Delta TL^3}{\mathrm{Ra}}}, \qquad \kappa = \frac{\nu}{\mathrm{Pr}} = \sqrt{\frac{\alpha g\Delta TL^3}{\mathrm{Pr}\cdot\mathrm{Ra}}}. \tag{27}$$

In a given system, Pr, Ra, ΔT, and L are specified, therefore the above equations lead to two equations for αg depending on the relaxation rate s_ν (through ν) and parameter a in the equilibrium of $n_3^{(\mathrm{eq})}$ in Eq. (14) (through κ), respectively. Consideration of numerical stability affects the choices of the value of s_ν. Once the value s_ν, so is the value of αg, and in turn the value of the parameter a. In this way the values of all the necessary parameters in the TLBE system are fully determined so simulations can be carried out.

The characteristic velocity in thermal convective flows is

$$U = \sqrt{\alpha g\Delta TL} = \sqrt{\frac{\mathrm{Ra}}{\mathrm{Pr}}}\frac{\nu}{L}. \tag{28}$$

The Mach number based on U should be small in order to comply with incompressible approximation of the flow and also the stability criterion on ν. Suppose that $U/c_s < \mathrm{Ma}^*$ for some critical Mach number Ma^* (usually $\mathrm{Ma}^* < 0.3$), then the viscosity ν has the following upper bound

$$\nu < \frac{\mathrm{Ma}^*}{\sqrt{3}}\sqrt{\frac{\mathrm{Pr}}{\mathrm{Ra}}}L, \tag{29}$$

where the length L is measured in the lattice unit $\delta x = 1$.

2.2. Implementation of TLBE and its boundary conditions

In the TLBE model boundary conditions are needed for both velocity $\boldsymbol{u}$ and temperature T. For the velocity field, we use no-slip boundary conditions which can be accurately realized by the bounce-back (BB) boundary conditions (BCs). For an impenetrable rigid wall aligned with a grid line and at the rest, the BB-BCs are:

$$f_{\bar{\imath}}(\boldsymbol{x}_f, t_n + \delta t) = f_i^*(\boldsymbol{x}_f, t_n), \tag{30}$$

where $\boldsymbol{x}_f$ is a fluid node adjacent to a boundary, $f_{\bar{\imath}}$ corresponds to $\boldsymbol{c}_{\bar{\imath}} = -\boldsymbol{c}_i$, $f_i^*(\boldsymbol{x}_f, t_n)$ denotes post-collision value of $f_i(\boldsymbol{x}_f, t_n)$, and $\boldsymbol{c}_{\bar{\imath}}$ is not parallel to the wall. Thus, the incoming distribution function (from domain outside of the wall) $f_{\bar{\imath}}(\boldsymbol{x}_f, t_n + \delta t)$ is equal to the outgoing distribution function (from the fluid domain) $f_i^*(\boldsymbol{x}_f, t_n)$.

As for the temperature field, two types of boundary conditions are needed: constant temperature and adiabatic, *i.e.*, $\hat{\boldsymbol{n}} \cdot \nabla\theta = 0$, where $\hat{\boldsymbol{n}}$ is unit vector out-normal to the wall. For a wall with the (dimensionless) temperature θ_w, the following "anti-bounce-back" boundary conditions for g_i are used:

$$g_{\bar{i}}(\boldsymbol{x}_f, t_n + \delta t) = -g_i^*(\boldsymbol{x}_f, t_n) + \frac{(4+a)}{10}\theta_w = -g_i^*(\boldsymbol{x}_f, t_n) + 2\sqrt{3}\kappa\theta_w, \tag{31}$$

where Eq. (16) has been substituted and, again, and $\boldsymbol{c}_{\bar{i}}$ is not parallel to the wall. An adiabatic wall, which is the Neumann boundary condition, can be realized with the bounce-back boundary conditions:

$$g_{\bar{i}}(\boldsymbol{x}_f, t_n + \delta t) = g_i^*(\boldsymbol{x}_f, t_n). \tag{32}$$

Periodic boundary conditions in the horizontal direction can also be used. We will study the effects due to different boundary conditions.

We would like to emphasize that it is imperative to use the MRT-TLBE in the simulations. With the bounce-back boundary conditions, we must use the relationships between the relaxation rates, that is $s_q(s_\nu)$ of Eq. (9) and $\sigma_\nu(\sigma_\kappa)$ of Eq. (17). These relationships ensure that the imposed boundary conditions for $\boldsymbol{u}$ and T are satisfied coincidentally at the location $\delta x/2$ beyond the last fluid node, and the location of the boundary conditions is independent of the transport coefficients. For the single-relaxation-time or lattice Bhatnagar–Gross–Krook (LBGK) models, the boundary location depends on the relaxation time τ, which is a significant source of error in the LBGK model.

The MRT-TLBE including the forcing term in Eq. (2) is implemented as follows:

1. Advection of $\{f_i\}$ and $\{g_i\}$;
2. Compute conserved quantities $\delta\rho$ and $\boldsymbol{u}$ from $\{f_i\}$, T from $\{g_i\}$, and other moments of $\{f_i\}$ and $\{g_i\}$;
3. Compute $\boldsymbol{u}^* = \boldsymbol{u} + \boldsymbol{a}(T)\delta t/2$, where $\boldsymbol{a}(T) := \boldsymbol{F}(T)/\rho_0$, and $\boldsymbol{F}$ is given by Eq. (23);
4. Compute equilibrium moments $\{m^{(\text{eq})}\}$ using $\delta\rho$ and $\boldsymbol{u}^*$, and $\{n^{(\text{eq})}\}$ using T;
5. Relax the moments $\{m_i\}$ and $\{n_i\}$;
6. Update $\boldsymbol{u}^{**} = \boldsymbol{u}^* + \boldsymbol{a}(T)\delta t/2 = \boldsymbol{u} + \boldsymbol{a}(T)\delta t$;
7. Map moments $\{m_i\}$ (which include $\boldsymbol{u}^{**}$) and $\{n_i\}$ to distribution functions $\{f_i\}$ and $\{g_i\}$, respectively;
8. Compute the post-collision distributions.

Two remarks are in order here. First, the relaxation rate for the momentum $\rho_0\boldsymbol{u}$ is unity in the MRT-LBE implementation regardless the values of the other relaxation rates, as implied S of Eq. (8), consequently there is no need to correct the artifacts in the LBGK model due to the inadvertent yet inevitable factor τ^{-1} in the forcing term [37], which affects the stress in the following time step. And second, the splitting of the forcing in two halves is similar to Strang splitting which ensures the second-order accuracy of the LBE scheme [29].

The flow domain used in this work is a rectangle of size $L \times H$. The mesh is a uniform Cartesian grid of size $(N_x + 2) \times (N_y + 2)$, so that $0 \le i \le (N_x + 1)$ and $0 \le j \le (N_y + 1)$. The fluid nodes are those of $1 \le i \le N_x$ and $1 \le j \le N_y$. Thus we have $L_{x,y} = N_{x,y}\delta x$ in lattice units. The external nodes of the mesh, *i.e.*, $i = 0$, $i = (N_x + 1)$, $j = 0$, and $j = (N_y + 1)$, are used as storage cells for the outgoing distribution functions during the advection step. Because the boundary conditions are satisfied at the location $\delta x/2$ beyond the last fluid nodes.

3. Square cavity with differentially heated vertical walls

3.1. Flow configurations and conditions

The first case to be simulated by the MRT-TLBE is the natural convection in a two-dimensional square cavity heated differentially on the vertical side walls. The flow configuration is illustrated in Fig. 1 and detailed as the following. The flow domain is a square of unit dimensions, *i.e.*, $(x, y) \in [0, 1] \times [0, 1]$. The direction of gravity is vertical and downward. The left and right vertical boundaries are maintained at a constant high temperature $\theta = +0.5$ and a constant low temperature $\theta = -0.5$, respectively; and the top and bottom boundaries are adiabatic, $\partial_y\theta = 0$. All boundaries are impenetrable, rigid and no-slip. Thus, for $\{g_i\}$, the BCs for constant-temperature and adiabatic walls are applied to the vertical and horizontal walls, respectively; and for $\{f_i\}$, the bounce-back boundary conditions are applied to all walls.

The initial state of the flow is quiescent and isothermal, *i.e.*, $\boldsymbol{u} = \boldsymbol{0}$, $\delta\rho = 0$, and $\theta = 0$. The criteria of attaining a steady state are:

$$\frac{\sum_{i,j} \|\boldsymbol{u}(i,j,t_{n+1000}) - \boldsymbol{u}(i,j,t_n)\|_2}{\sum_{i,j} \|\boldsymbol{u}(i,j,t_{n+1000})\|_2} < 10^{-12}, \tag{33a}$$

$$\max_{i,j} |\theta(i,j,t_{n+1000}) - \theta(i,j,t_n)| < 10^{-6}, \tag{33b}$$

where $\|\cdot\|_2$ denotes the L_2 norm.

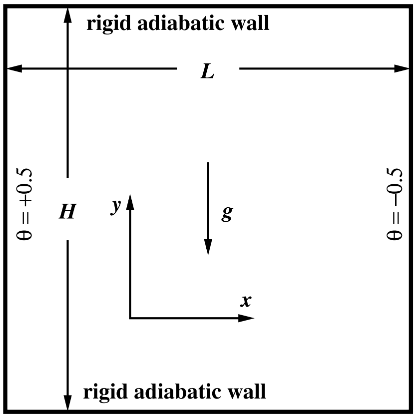

Fig. 1. Illustration of the flow domain for the square cavity ($H = L$) with differentially heated side walls.

Unless otherwise stated, the parameter a in κ of Eq. (16) and the viscosity ν are determined by the following formulas:

$$a = \frac{20\mathrm{Ma}N_x}{\sqrt{\mathrm{Ra\ Pr}}} - 4, \qquad \nu = \sqrt{\frac{3.6}{\mathrm{Ra}}}c\delta x, \tag{34}$$

where the formula of a is derived from Eq. (27) for κ, and the formula for ν is obtained based on the following considerations. To ensure the stability with the smallest mesh size $N = 41$ in our simulations, we use Pr $= 0.71$ and a reasonable value of the Mach number in Eq. (29) to obtain the above upper-bound for ν.

3.2. Quantities under study

This flow has been extensively studied as a bench-mark flow [38] with various numerical methods including finite-difference (FD) [39,40], finite-element (FE) [41], finite-volume (FV) [42,43], and pseudo-spectral (PS) [44–46], spectral-element (SE) [47], and other methods [38]. The paper by De Vahl Davis [39] is a comprehensive review of this flow, which provides a guide to our work. We will compute some quantities of interest and compare our results with existing data. We will use Pr $= 0.71$ (for air) and Ra $= 10^3$, 10^4, 10^5, and 10^6. The quantities to be computed include averaged and local Nusselt numbers. The local heat flux in the horizontal (x) direction is

$$q_x = u\theta - \partial_x\theta, \tag{35}$$

which will be used to compute Nusselt numbers. The first is the volume average Nusselt number $\langle\mathrm{Nu}\rangle$,

$$\langle\mathrm{Nu}\rangle = \frac{1}{LH\Delta\theta}\int_0^L \mathrm{d}x \int_0^H \mathrm{d}y\, q_x \approx \frac{1}{N_xN_y\Delta\theta}\sum_{i,j=1}^{N_x,N_y} q_x(i,j), \tag{36}$$

where $\Delta\theta = 1$. The second and third ones are the average Nusselt numbers along the hot wall at $x = 0$ and the vertical mid-plane of the cavity at $x = 1/2$:

$$\langle\mathrm{Nu}\rangle_0 \approx \frac{1}{N_y\Delta\theta}\sum_{j=1}^{N_y} q_x(i,j)|_{x=0}, \tag{37a}$$

$$\langle\mathrm{Nu}\rangle_{1/2} \approx \frac{1}{N_y\Delta\theta}\sum_{j=1}^{N_y} q_x(i,j)|_{x=1/2}. \tag{37b}$$

In addition, we also identify the maximum and minimum local Nusselt number, $\mathrm{Nu}_{\max}$ and $\mathrm{Nu}_{\min}$, at the left wall ($x = 0$) and their (normalized) vertical coordinates y. Note that in Eq. (37a), $x = 0$ is the location of the left vertical wall, which is located at $\delta x/2$ beyond the last fluid nodes, $\{i = 1, N_x | 1 \le j \le N_y\}$ and $\{j = 1, N_y | 1 \le i \le N_x\}$, as discussed previously. The derivative $\partial_x\theta$ needed for the Nusselt numbers is approximated by the finite difference formula involving nine points including (i, j), $(i \pm 1, j)$, $(i, j \pm 1)$, and $(i \pm 1, j \pm 1)$.

The values of some hydrodynamic variables and their locations are of interest, too; they include the maximum horizontal velocity $u_{\max}$ on the vertical mid-plane of the cavity and its y coordinate, the maximum vertical velocity $v_{\max}$ on the horizontal mid-plane and its x coordinate, the maximum absolute value of the stream function and its location, $|\psi|_{\max}$, and the absolute value of the stream function in the center of the cavity, $|\psi_{\mathrm{mid}}|$. In the ensuing simulations, the velocity field $\boldsymbol{u}$ is normalized by κ/L_y.

Table 1
Ra dependence of L_2-normed grid convergence of flow fields. Pr = 0.71 and Ma = 0.01.

Ra	10^3	10^4	10^5	10^6
N^2	$\Vert\delta\boldsymbol{u}\Vert_2$			
41^2	$2.523 \cdot 10^{-3}$	$4.359 \cdot 10^{-3}$	$1.341 \cdot 10^{-2}$	$4.580 \cdot 10^{-2}$
81^2	$6.378 \cdot 10^{-4}$	$1.118 \cdot 10^{-3}$	$3.483 \cdot 10^{-3}$	$1.178 \cdot 10^{-2}$
161^2	$1.317 \cdot 10^{-4}$	$2.329 \cdot 10^{-4}$	$7.334 \cdot 10^{-4}$	$2.494 \cdot 10^{-3}$
n	2.1589	2.1420	2.1246	2.1278
	$\Vert\delta p\Vert_2$			
41^2	$3.111 \cdot 10^{-3}$	$2.832 \cdot 10^{-3}$	$4.329 \cdot 10^{-3}$	$9.929 \cdot 10^{-3}$
81^2	$8.615 \cdot 10^{-4}$	$8.214 \cdot 10^{-4}$	$1.164 \cdot 10^{-3}$	$2.859 \cdot 10^{-3}$
161^2	$1.949 \cdot 10^{-4}$	$1.919 \cdot 10^{-4}$	$2.579 \cdot 10^{-4}$	$6.000 \cdot 10^{-4}$
n	2.0254	1.9681	2.0621	2.0520
	$\Vert\delta\theta\Vert_2$			
41^2	$3.590 \cdot 10^{-4}$	$1.158 \cdot 10^{-3}$	$4.831 \cdot 10^{-3}$	$1.564 \cdot 10^{-2}$
81^2	$8.555 \cdot 10^{-5}$	$2.785 \cdot 10^{-4}$	$1.154 \cdot 10^{-3}$	$3.819 \cdot 10^{-3}$
161^2	$1.713 \cdot 10^{-5}$	$5.603 \cdot 10^{-5}$	$2.312 \cdot 10^{-4}$	$7.709 \cdot 10^{-4}$
n	2.2247	2.2144	2.2224	2.2008

3.3. Grid convergence of flow fields

We use a uniform mesh of size $N_x \times N_y = N^2$ with N^2 between 41^2 and 321^2 to investigate the convergence behavior of the MRT-TLBE. The grid spacing h is then $1/N$. Another parameter considered here is the Mach number Ma, which is effectively equivalent to the Courant–Friedrichs–Lewy (CFL) number as far as the time step size is concerned [18]. Of course, the Mach number is also directly related to the compressibility error in the LBE [48–50,18]. We first study the convergence behavior of the MRT-TLBE with a fixed Mach number Ma = 0.01. The error in the velocity field is computed as follows,

$$\Vert\delta\boldsymbol{u}\Vert_2 := \frac{\sum_j \Vert\boldsymbol{u}(\boldsymbol{x}_j) - \boldsymbol{u}^*(\boldsymbol{x}_j)\Vert_2}{\sum_j \Vert\boldsymbol{u}^*(\boldsymbol{x}_j)\Vert_2}, \tag{38}$$

where $\boldsymbol{u}^*(\boldsymbol{x}_j)$ is the reference solution of the velocity field. The errors for the pressure p and temperature θ are similarly defined. We use the solutions obtained with $N^2 = 321^2$ as the reference solutions. It should be noted that, because the boundary conditions are satisfied $h/2$ beyond the last fluid nodes, the meshes of different size N^2 have no overlapping grid points. Thus, the flow fields obtained with the largest mesh size $N^2 = 321^2$ are interpolated to coarser meshes with a second-order interpolation in both x and y direction to compute the differences of flow fields.

In Table 1 we tabulate the L_2-normed errors of the velocity $\boldsymbol{u}$, pressure p, and (normalized) temperature θ, as well as the rates (n) of convergence of these flow fields. The rates of convergence for the flow fields are all about 2.0. However, if we do not interpolate the flow fields and simply compute the difference of the flow fields with different meshes on the closest grid points, the rates of convergence would be between 1.3 and 1.4. We also notice that the errors of the flow fields depend on the Rayleigh number Ra. With a fixed resolution N, the errors in the velocity $\boldsymbol{u}$, the pressure p, and the temperature θ increase with Ra except for the case of $\Vert\delta p\Vert_2$ with Ra $= 10^4$.

3.4. Convergence of Nusselt numbers

We study convergence behaviors of the local and averaged Nusselt numbers. For various Nusselt numbers, we need to compute the heat flux q_x of Eq. (35) at boundaries, which are located at $\delta x/2$ beyond the last fluid nodes. Since the vertical walls are no-slip ones, the Nusselt number Nu at the left wall is given by $-\partial_x\theta$; the temperature gradient $\partial_x\theta$ along each horizontal lattice line is evaluated at $x = 0$ with the temperature θ at $x = 0$, and $i = 1$ and 2. The temperature θ at the horizontal walls is unknown and is obtained by fitting the first four points next to the walls along each vertical lattice line with a second-order polynomial $a + b(y - y_0)^2$, where y_0 is the vertical position of a horizontal wall.

Fig. 3 shows the Nusselt number averaged over vertical grid lines, $\langle \mathrm{Nu}\rangle_y$, and the local Nusselt number at the left (hot) wall $x = 0$, with Ra $= 10^6$. Note that the average Nusselt number $\langle \mathrm{Nu}\rangle_y$ is symmetric about the vertical center line of the cavity $x = 1/2$, we only show $\langle \mathrm{Nu}\rangle_y$ in the interval of $0 \le x \le 1/2$. We can see that $\langle \mathrm{Nu}\rangle_y$ oscillates severely near the wall when the mesh size N^2 is small. With the largest mesh size $N^2 = 321^2$, $\langle \mathrm{Nu}\rangle_y$ converges to a constant. However a small oscillation remains near the wall. The Nusselt number Nu at the hot wall should have a minimum at the top left corner $(x, y) = (0, 1)$. It can be seen that Nu oscillates slightly near the top left corner when the mesh size is small.

We tabulate average and local Nusselt numbers and their locations depending on the Rayleigh number Ra and mesh size N^2 in Table 2. The value of $\mathrm{Nu}_{\max}$ is found by using the least-square fit of five points about $\mathrm{Nu}_{\max}$ with a third-order

Table 2
Convergence behavior of the Nusselt numbers with Pr = 0.71 and Ma = 0.01. The asymptotic values of the Nusselt numbers obtained by Eq. (39) and order of convergence are given in the rows with ∞ and n, respectively. The data marked with "$*$" are not used in the calculations of the corresponding asymptotic values.

Ra	N^2	$\langle \mathrm{Nu}\rangle$	Nu_0	$\mathrm{Nu}_{1/2}$	Nu_{max}	y	Nu_{min}
10^3	41^2	1.1172	1.1177	1.1176	1.5099*	0.09381*	0.6905
	57^2	1.1175	1.1177	1.1177	1.5082	0.09036	0.6910
	81^2	1.1176	1.1178	1.1177	1.5072	0.08922	0.6911
	113^2	1.1177	1.1178	1.1178	1.5068	0.08877	0.6912
	161^2	1.1178	1.1178	1.1178	1.5065	0.08858	0.6912
	225^2	1.1178	1.1178	1.1178	1.5064	0.08850	0.6912
	321^2	1.1178	1.1178	1.1178	1.5064	0.08846	0.6912
	∞	1.1178	1.1178	1.1178	1.5063	0.08843	0.6912
	n	1.9907	1.8058	1.9440	2.0086	2.4485	2.7541
10^4	41^2	2.2407	2.2476	2.2393	3.5857	0.1395	0.5869
	57^2	2.2427	2.2460	2.2419	3.5583	0.1414	0.5863
	81^2	2.2437	2.2453	2.2434	3.5441	0.1428	0.5858
	113^2	2.2443	2.2450	2.2440	3.5375	0.1435	0.5854
	161^2	2.2445	2.2449	2.2444	3.5342	0.1439	0.5852
	225^2	2.2447	2.2449	2.2446	3.5326	0.1440	0.5851
	321^2	2.2447	2.2448	2.2447	3.5318	0.1441	0.5850
	∞	2.2448	2.2448	2.2448	3.5310	0.1443	0.5849
	n	1.9739	2.3282	2.0193	2.0369	1.7297	1.6019
10^5	41^2	4.5051	4.5511	4.5063	8.2585	0.07487	0.7853
	57^2	4.5128	4.5348	4.5135	8.0027	0.07495	0.7601
	81^2	4.5171	4.5270	4.5175	7.8549	0.07738	0.7449
	113^2	4.5193	4.5239	4.5195	7.7861	0.07952	0.7375
	161^2	4.5205	4.5226	4.5206	7.7512	0.08082	0.7325
	225^2	4.5210	4.5220	4.5211	7.7355	0.08146	0.7302
	321^2	4.5213	4.5218	4.5214	7.7275	0.08179	0.7290
	∞	4.5216	4.5214	4.5216	7.7161	0.08238	0.7279
	n	1.9424	2.1385	1.9620	1.9106	1.3529	1.9237
10^6	41^2	8.8106	9.0356	8.8600	21.1647*	0.04086*	1.0019*
	57^2	8.8138	8.9487	8.8400	20.0506*	0.03738*	1.1912*
	81^2	8.8183	8.8840	8.8317	18.9821*	0.03747*	1.1227
	113^2	8.8213	8.8518	8.8283	18.3065	0.03539	1.0582
	161^2	8.8232	8.8362	8.8267	17.9028	0.03650	1.0182
	225^2	8.8241	8.8299	8.8259	17.7147	0.03769	0.9988
	321^2	8.8247	8.8272	8.8256	17.6196	0.03846	0.9886
	∞	8.8253	8.8192	8.8254	17.5274	0.03952	0.9769
	n	1.5421	1.6861	2.5344	2.0471	1.3224	1.8474

polynomial of y locally. The value of Nu_{min} is always located at 2–3 grid spacings away from the top left corner, thus we may assume the location converges to $y = 1$ and do not list it in Table 2. In Table 2 we also give the asymptotic values of Nusselt numbers, which are obtained by the least-square fit with the following third-order polynomial:

$$f(h) = a_0 + a_2 h^2 + a_3 h^3, \tag{39}$$

where $h := 1/N$ is the (normalized) grid spacing, and a_0 is the asymptotic value of $f(h)$ in the limit of $h \to 0$ (or $N \to \infty$). The asymptotic values of the Nusselt numbers are then used to compute the rates of convergence n. It should be noted that for both Nu_{max} and Nu_{min}, the rates of convergence are measured with L_∞ norm.

As shown in Table 2, all the average and local Nusselt numbers exhibit monotonic behavior as the mesh size N^2 increases. This monotonicity is preserved by the polynomial of Eq. (39) in the relevant range of h. In the case of the lowest Rayleigh number, $\mathrm{Ra} = 10^3$, it can be seen clearly that the Nusselt numbers quickly reach their asymptotic values independent of grid-size h. In some cases the data obtained with the coarsest meshes do not fit well with the polynomial (39), thus these data are excluded in the least-square fitting. We observe that in most cases, a second-order convergence is achieved for the Nusselt numbers. The worst rate of convergence corresponds to the vertical location y of Nu_{max} with $\mathrm{Ra} = 10^5$ and 10^6. Also, the convergence rates for $\langle \mathrm{Nu}\rangle$ and Nu_0 with $\mathrm{Ra} = 10^6$ are less than 2.0.

3.5. Convergence of hydrodynamic quantities

In Table 3 we tabulate the value of the stream-function at the center of the cavity, $|\psi_{mid}|$, and the maximum value of the stream-function, $|\psi|_{max}$, and its location, the maximum x velocity on the vertical center line $x = 1/2$, u_{max}, and its y coordinate, and the maximum y velocity on the horizontal center line $y = 1/2$, v_{max}, and its x coordinate, as well as the asymptotic values of $|\psi_{mid}|$, $|\psi|_{max}$, u_{max}, and v_{max}, and the corresponding rates of convergence n. The asymptotic values

Table 3
Convergence behavior of the hydrodynamic variables with Pr = 0.71 and Ma = 0.01. The data marked with "∗" are not used in the calculations of the corresponding asymptotic values.

Ra	N^2	$\lvert\psi_{\mathrm{mid}}\rvert$	$\lvert\psi\rvert_{\max}$	(x, y)	$u_{\max}$	y	$v_{\max}$	x
10^3	41^2	1.1702	–	–	3.6439	0.8133	3.6935	0.1788
	57^2	1.1724	–	–	3.6466	0.8133	3.6954	0.1786
	81^2	1.1735	–	–	3.6480	0.8132	3.6964	0.1784
	113^2	1.1741	–	–	3.6487	0.8132	3.6969	0.1784
	161^2	1.1744	–	–	3.6491	0.8132	3.6972	0.1784
	225^2	1.1745	–	–	3.6493	0.8132	3.6973	0.1783
	321^2	1.1746	–	–	3.6494	0.8132	3.6974	0.1783
	∞	1.1746	–	–	3.6494	0.8132	3.6974	0.1783
	n	2.0140	–	–	1.9833	1.9180	1.9587	1.9183
10^4	41^2	5.0590	–	–	16.1848	0.8231	19.6052	0.1195
	57^2	5.0662	–	–	16.1839	0.8232	19.6160	0.1192
	81^2	5.0701	–	–	16.1836	0.8232	19.6221	0.1190
	113^2	5.0718	–	–	16.1835	0.8232	19.6250	0.1190
	161^2	5.0728	–	–	16.1834	0.8232	19.6266	0.1189
	225^2	5.0732	–	–	16.1834	0.8232	19.6274	0.1189
	321^2	5.0735	–	–	16.1834	0.8232	19.6278	0.1189
	∞	5.0737	–	–	16.1833	0.8232	19.6282	0.1189
	n	2.0269	–	–	3.0339	1.6742	1.9684	1.9594
10^5	41^2	9.0598	9.5781	(0.2970, 0.5962)	34.9560*	0.8525*	68.4396	0.06708
	57^2	9.0876	9.5900	(0.2919, 0.5988)	34.7997*	0.8531*	68.5277	0.06648
	81^2	9.1022	9.6019	(0.2881, 0.6001)	34.7837	0.8539	68.5819	0.06618
	113^2	9.1089	9.6094	(0.2864, 0.6008)	34.7586	0.8542	68.6070	0.06602
	161^2	9.1123	9.6136	(0.2854, 0.6012)	34.7495	0.8544	68.6212	0.06594
	225^2	9.1139	9.6151	(0.2850, 0.6013)	34.7456	0.8545	68.6280	0.06590
	321^2	9.1148	9.6160	(0.2847, 0.6014)	34.7430	0.8546	68.6318	0.06588
	∞	9.1157	9.6179	(0.2843, 0.6015)	34.7424	0.8546	68.6358	0.06586
	n	2.0328	1.5571	(1.7293, 1.9795)	2.8793	1.7545	1.8989	2.0363
10^6	41^2	16.2422	16.6153*	(0.1779, 0.5455)*	64.4482	0.8421	218.1669*	0.04161*
	57^2	16.3184	16.7160*	(0.1636, 0.5473)*	64.6332	0.8459	220.4276*	0.03916*
	81^2	16.3553	16.7254	(0.1587, 0.5453)	64.7319	0.8481	220.4059	0.03843
	113^2	16.3716	16.7614	(0.1548, 0.5457)	64.7810	0.8490	220.4684	0.03807
	161^2	16.3797	16.7885	(0.1525, 0.5462)	64.8077	0.8495	220.5105	0.03791
	225^2	16.3832	16.8012	(0.1514, 0.5466)	64.8206	0.8497	220.5363	0.03783
	321^2	16.3849	16.8057	(0.1509, 0.5466)	64.8277	0.8498	220.5506	0.03779
	∞	16.3868	16.8149	(0.1503, 0.5468)	64.8336	0.8499	220.5658	0.03776
	n	2.1299	1.7145	(1.9074, 1.4639)	2.0167	1.9639	1.7157	2.2580

are obtained by the least-square fitting with the third-order polynomial of Eq. (39), similar to what we did with the data in Table 2. Note that when Ra $= 10^3$ and 10^4, the position of $\lvert\psi_{\mathrm{mid}}\rvert$ coincides with that of $\lvert\psi\rvert_{\max}$, as exhibited by the corresponding streamlines in Fig. 2.

The values of both $\lvert\psi_{\mathrm{mid}}\rvert$ and $\lvert\psi\rvert_{\max}$ increase monotonically as the mesh size N^2 increases. The rate of convergence for $\lvert\psi_{\mathrm{mid}}\rvert$ is about 2.0, while that for $\lvert\psi\rvert_{\max}$ and its coordinates are lower. As for $u_{\max}$ and $v_{\max}$ as well as their locations, the rates of convergence are about 2.0 in most cases. The data in Tables 1–3 clearly indicate that the MRT-TLBE scheme has a second-order rate of convergence.

3.6. Mach-number effect

The LBE is based on small-Mach-number expansions of the Maxwellian equilibrium [10,11] and the errors in flow fields depend on the Mach number Ma indicating the presence of compressibility effect [48–50,18]. We will study the effect of the Mach number Ma on the flow fields and other quantities under study. We will fix Ra $= 10^6$ and Pr $= 0.71$ in what follows unless otherwise stated.

First, we use the flow fields obtained with the smallest Mach number Ma $= 0.01$ and the largest mesh size $N^2 = 321^2$ as the reference fields to compute the errors in the velocity $\boldsymbol{u}$, pressure p, and temperature θ, *i.e.*, the reference field $\boldsymbol{u}^*$ in Eq. (38) is the one obtained with Ma $= 0.01$ and $N^2 = 321^2$. The results are tabulated in Table 4. We observe that the errors in $\boldsymbol{u}$, p, and θ are independent of Ma for $N^2 < 321^2$, and the rates of convergence for all flow fields are about 2.0, clearly indicating a second-order convergence.

To further investigate the effect of Ma on the flow fields, we compute the relative flow field differences with respect to their solutions obtained with Ma $= 0.01$ and a fixed mesh size N^2. That is, with a fixed mesh size N^2, we compute the flow fields depending on Ma, then compute the flow field differences with the same resolution with respect to the solutions of Ma $= 0.01$. The results are tabulated in Table 5. As can be seen clearly, the flow field differences with an equal resolution

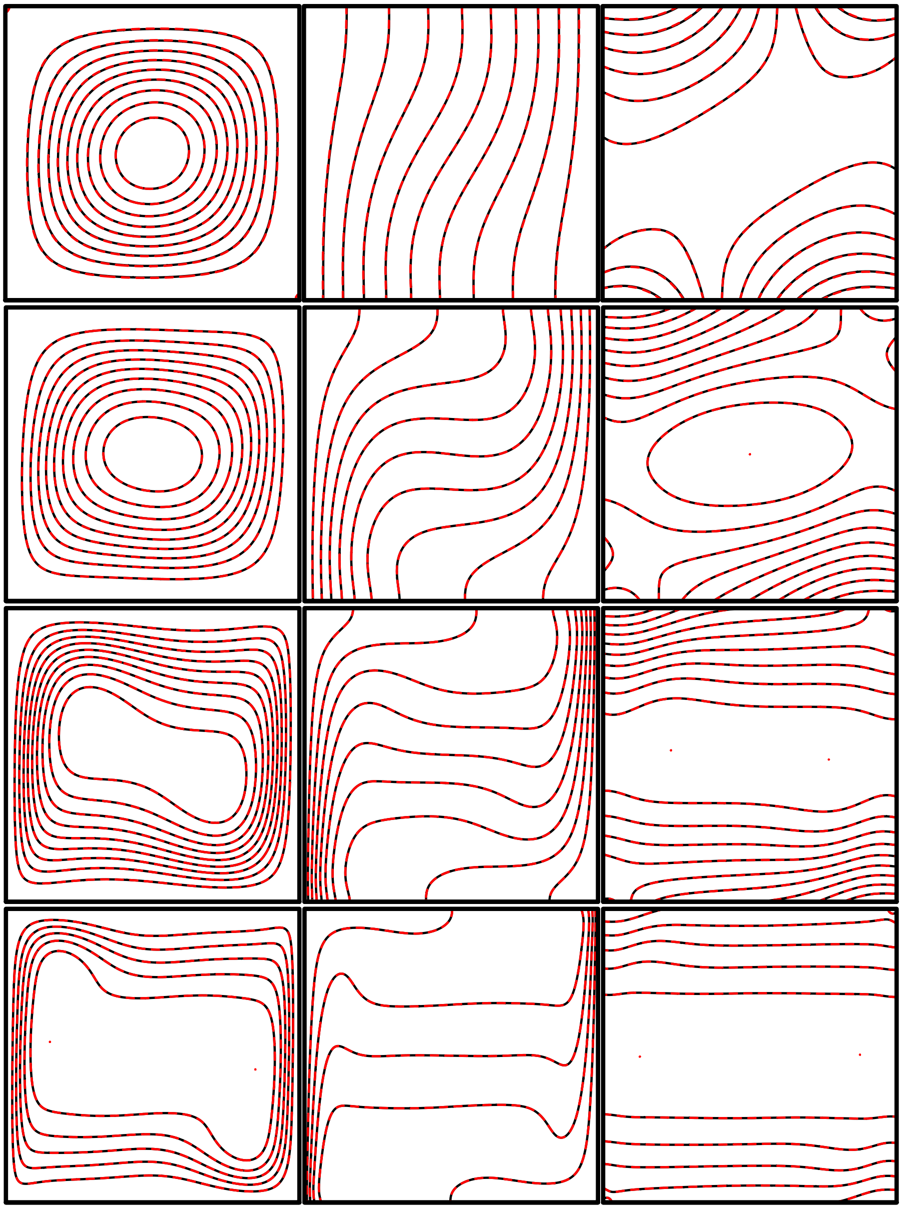

Fig. 2. Flow fields in the square cavity with differentially heated vertical walls and $\Pr = 0.71$: the streamlines ψ (left), isotherms (middle), and pressure p (right). From top to bottom: $\mathrm{Ra} = 10^3$, 10^4, 10^5, and 10^6. Mesh sizes: $N^2 = 161^2$ for $\mathrm{Ra} = 10^3$ and $N^2 = 321^2$ for $\mathrm{Ra} \geq 10^4$. Solid (red) lines: $\mathrm{Ma} = 0.01$, and dashed (black) lines: $\mathrm{Ma} = 0.02$ for $\mathrm{Ra} = 10^3$, $\mathrm{Ma} = 0.05$ for $\mathrm{Ra} = 10^4$, and $\mathrm{Ma} = 0.15$ for $\mathrm{Ra} \geq 10^5$. (For interpretation of the references to colour in this figure legend, the reader is referred to the web version of this article.)

N and different Mach number Ma are rather weak—they all remain in the order of 10^{-7} or smaller. It can also be seen that except for the case of $\|\delta \boldsymbol{u}\|$ with $N^2 = 41^2$, the differences between flow fields increase when both N and Ma increase, although the effect of Ma on the temperature field θ seems to be weaker.

In Table 6 we show the effect of Mach number Ma on local hydrodynamic quantities $u_{\max}$ and $v_{\max}$ as well as the local Nusselt number $\mathrm{Nu}_{\max}$. The Mach number Ma has very little, if any, effect on these quantities. With a fixed mesh size N^2, the effect of Ma on $u_{\max}$ appears in the seventh significant digit, and that on $v_{\max}$ and $\mathrm{Nu}_{\max}$ appears in the eighth significant digit. This clearly suggests that Mach number effects on these quantities are insignificant and negligible. We observe that the rates of convergence for both $u_{\max}$ and $\mathrm{Nu}_{\max}$ are about 2.0, while that for $v_{\max}$ is only about 1.7. We also notice that the magnitude of $v_{\max}$ is the largest among $u_{\max}$, $v_{\max}$, and $\mathrm{Nu}_{\max}$. Because the Mach number in the LBE is effectively the CFL number [18], which affects the time step size thus the computational speed, one should use as large a Mach number as possible to enhance computational efficiency, so long as both accuracy and stability are maintained.

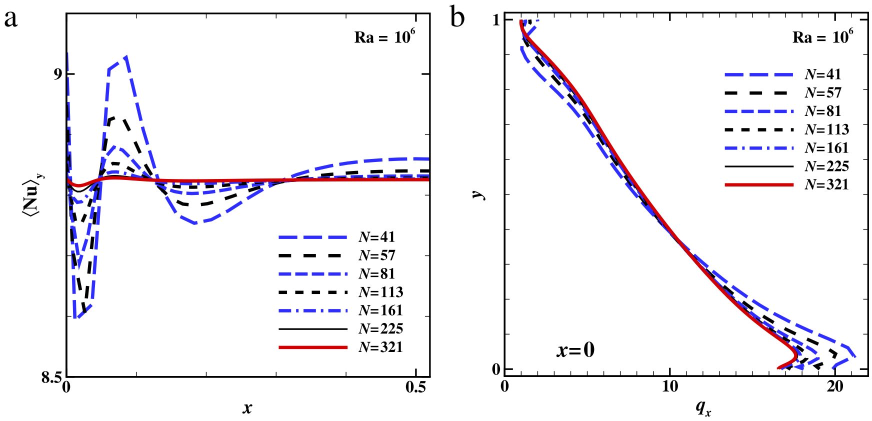

Fig. 3. (a) Distribution of the Nusselt number $\langle \mathrm{Nu} \rangle_y$ averaged over y as a function of x. $\langle \mathrm{Nu} \rangle_y$ is symmetric about $x = 1/2$. (b) Distribution of the heat flux $q_x(y)$ on the left (hot) wall $x = 0$. $\mathrm{Ra} = 10^6$ and $\mathrm{Ma} = 0.01$.

Table 4
Mach-number dependence of the errors in flow fields $\boldsymbol{u}$, p, θ with L_2-norm. $\mathrm{Ra} = 10^6$ and $\mathrm{Pr} = 0.71$. The flow fields with $N^2 = 321^2$ and $\mathrm{Ma} = 0.01$ are used as the reference solutions to compute the errors.

Ma	0.01	0.02	0.05	0.10	0.15
N^2	$\Vert\delta \boldsymbol{u}\Vert_2$				
41^2	$4.5799504 \cdot 10^{-2}$	$4.5799509 \cdot 10^{-2}$	$4.5799515 \cdot 10^{-2}$	$4.5799514 \cdot 10^{-2}$	$4.5799513 \cdot 10^{-2}$
81^2	$1.1777526 \cdot 10^{-2}$	$1.1777518 \cdot 10^{-2}$	$1.1777514 \cdot 10^{-2}$	$1.1777512 \cdot 10^{-2}$	$1.1777509 \cdot 10^{-2}$
161^2	$2.4943359 \cdot 10^{-3}$	$2.4943174 \cdot 10^{-3}$	$2.4943087 \cdot 10^{-3}$	$2.4943045 \cdot 10^{-3}$	$2.4942981 \cdot 10^{-3}$
321^2	–	$1.7684115 \cdot 10^{-7}$	$2.6032163 \cdot 10^{-7}$	$3.0046556 \cdot 10^{-7}$	$3.6062902 \cdot 10^{-7}$
n	2.1278332	2.1278387	2.1278414	2.1278426	2.1278445
	$\Vert\delta p\Vert_2$				
41^2	$9.9289858 \cdot 10^{-3}$	$9.9289837 \cdot 10^{-3}$	$9.9289814 \cdot 10^{-3}$	$9.9289817 \cdot 10^{-3}$	$9.9289821 \cdot 10^{-3}$
81^2	$2.8593464 \cdot 10^{-3}$	$2.8593493 \cdot 10^{-3}$	$2.8593507 \cdot 10^{-3}$	$2.8593514 \cdot 10^{-3}$	$2.8593525 \cdot 10^{-3}$
161^2	$5.9995930 \cdot 10^{-4}$	$5.9996560 \cdot 10^{-4}$	$5.9996862 \cdot 10^{-4}$	$5.9997015 \cdot 10^{-4}$	$5.9997277 \cdot 10^{-4}$
321^2	–	$6.2892469 \cdot 10^{-8}$	$1.0319561 \cdot 10^{-7}$	$1.2599556 \cdot 10^{-7}$	$1.3729586 \cdot 10^{-7}$
n	2.0520076	2.0519997	2.0519959	2.0519940	2.0519909
	$\Vert\delta\theta\Vert_2$				
41^2	$1.5640836 \cdot 10^{-2}$	$1.5640836 \cdot 10^{-2}$	$1.5640835 \cdot 10^{-2}$	$1.5640836 \cdot 10^{-2}$	$1.5640836 \cdot 10^{-2}$
81^2	$3.8188514 \cdot 10^{-3}$	$3.8188519 \cdot 10^{-3}$	$3.8188522 \cdot 10^{-3}$	$3.8188524 \cdot 10^{-3}$	$3.8188525 \cdot 10^{-3}$
161^2	$7.7092667 \cdot 10^{-4}$	$7.7092763 \cdot 10^{-4}$	$7.7092821 \cdot 10^{-4}$	$7.7092843 \cdot 10^{-4}$	$7.7092888 \cdot 10^{-4}$
321^2	–	$2.8141413 \cdot 10^{-8}$	$4.7069431 \cdot 10^{-8}$	$5.6457606 \cdot 10^{-8}$	$6.1130623 \cdot 10^{-8}$
n	2.2007881	2.2007872	2.2007866	2.2007864	2.2007860

Clearly, the Mach number has little effect on the accuracy of the MRT-TLBE simulations for incompressible thermal flows with the Boussinesq approximation. This is in sharp contrast to athermal flows (cf., *e.g.*, [48,18]) in which the errors are of the order of Mach number square. The reason for this insensitivity of thermal flows to the Mach number is that, in thermal flows, the buoyancy force due to the temperature is driving flow, while the buoyancy force is realized through density variation, it is inherently different from the density fluctuations which are responsible for acoustic waves in athermal flows.

3.7. Computational efficiency

Our code is written in Fortran with MPI and runs on an IBM p5 575 system with nodes of 16 duo-core 1.9 GHz processors. With a mesh size $N^2 = 321^2$, the speed of our code on one processor is about $7.3 \cdot 10^6$ and $9.9 \cdot 10^6$ sites update per second with or without MPI.

Since the Mach number Ma has very little quantitative effect on the flow fields and hydrodynamic quantities under study, as shown in the previous section, the only concern is the numerical stability for computational efficiency. Because Mach number Ma is equivalent to the CFL number [18], thus the greater the Mach number, the larger the time step size, and hence the faster the computational speed. In Table 7 we show the number of iterations to achieve the steady state criteria given by Eqs. (33) depending on the Mach number Ma and the mesh size N^2. Clearly, with the Rayleigh number Ra fixed, the number of iterations N_t is proportional to the mesh size N and to Ma^{-1}.

Table 5
The Mach-number dependence of L_2-norm differences in flow fields with equal mesh size N^2. The flow fields obtained with Ma = 0.01 are used as the reference solutions.

Ma	0.02	0.05	0.10	0.15
N^2	$\|\delta \boldsymbol{u}(\mathrm{Ma})\|_2 \cdot 10^7$			
41^2	0.20222368	0.43706473	0.41168471	0.39348873
81^2	0.36606726	0.54019218	0.62654639	0.74492363
161^2	0.82486307	1.21813015	1.40795718	1.68678479
321^2	1.76841156	2.60321632	3.00465563	3.60629020
	$\|\delta p(\mathrm{Ma})\|_2 \cdot 10^7$			
41^2	0.15852664	0.29812073	0.34574955	0.36421706
81^2	0.23645841	0.39160877	0.48417119	0.51853590
161^2	0.38663073	0.63573719	0.78335873	0.84284211
321^2	0.62892469	1.03195616	1.25995569	1.37295864
	$\|\delta \theta(\mathrm{Ma})\|_2 \cdot 10^7$			
41^2	0.07039132	0.13246378	0.15329471	0.16184793
81^2	0.10665124	0.17819453	0.21795092	0.23075655
161^2	0.17341850	0.28760317	0.35006790	0.37356528
321^2	0.28141413	0.47069431	0.56457606	0.61130623

Table 6
The Mach-number dependence of the convergence of u_{max}, v_{max} and Nu_{max} for Ra $= 10^6$ and Pr = 0.71.

Ma	0.01	0.02	0.05	0.10	0.15
N^2	u_{max}				
41^2	64.44819215	64.44819357	64.44819531	64.44819498	64.44819462
57^2	64.63320164	64.63319843	64.63319472	64.63319509	64.63319567
81^2	64.73194665	64.73194324	64.73194161	64.73194074	64.73193963
113^2	64.78099738	64.78100152	64.78100338	64.78100584	64.78100465
161^2	64.80770630	64.80769867	64.80769502	64.80769316	64.80769061
225^2	64.82063061	64.82063999	64.82064420	64.82064625	64.82064975
321^2	64.82765313	64.82763694	64.82762932	64.82762546	64.82762006
∞	64.83357823	64.83357433	64.83357298	64.83357185	64.83356989
n	2.01669407	2.01623400	2.01598194	2.01588233	2.01578058
	v_{max}				
41^2	218.16693306	218.16693330	218.16693370	218.16693342	218.16693314
57^2	220.42757268	220.42757111	220.42756935	220.42756928	220.42756945
81^2	220.40585471	220.40585314	220.40585235	220.40585184	220.40585132
113^2	220.46842291	220.46842364	220.46842381	220.46842431	220.46842382
161^2	220.51054480	220.51054158	220.51053998	220.51053903	220.51053799
225^2	220.53629632	220.53629845	220.53629905	220.53629937	220.53630051
321^2	220.55058072	220.55057425	220.55057119	220.55056936	220.55056729
∞	220.56575230	220.56574691	220.56574425	220.56574241	220.56574132
n	1.71573997	1.71573860	1.71573946	1.71574888	1.71572896
	Nu_{max}				
41^2	21.16471995	21.16471988	21.16471980	21.16471979	21.16471978
57^2	20.05064995	20.05064990	20.05064986	20.05064983	20.05064981
81^2	18.98214565	18.98214559	18.98214555	18.98214552	18.98214552
113^2	18.30649044	18.30649032	18.30649025	18.30649017	18.30649017
161^2	17.90277648	17.90277642	17.90277636	17.90277632	17.90277632
225^2	17.71471420	17.71471401	17.71471390	17.71471383	17.71471378
321^2	17.61963289	17.61963284	17.61963277	17.61963273	17.61963273
∞	17.52743014	17.52743005	17.52742996	17.52742990	17.52742990
n	2.04712483	2.04712463	2.04712448	2.04712430	2.04712430

Next we consider the Rayleigh-number dependence of the number of iterations to achieve steady state. The Mach number Ma is fixed at 0.01 and the results are given in Table 8. Clearly, with the resolution N and the Mach number Ma fixed, the number of iterations N_t doubles approximately as Ra increases ten fold. Hence, asymptotically the number of iterations to reach steady state depends approximately on N, Ra and Ma as follows:

$$N_t \propto N \cdot \mathrm{Ra}^{\lg 2} \cdot \mathrm{Ma}^{-1}. \tag{40}$$

Table 7
The Mach-number dependence of the number of iterations to achieve steady state. Ra = 10^6 and Pr = 0.71.

N^2	Ma = 0.01	Ma = 0.02	Ma = 0.05	Ma = 0.10	Ma = 0.15
41^2	1,489,000	778,000	332,000	173,000	120,000
57^2	2,061,000	1,056,000	450,000	235,000	160,000
81^2	2,859,000	1,495,000	626,000	326,000	222,000
113^2	3,891,000	2,038,000	853,000	445,000	309,000
161^2	5,412,000	2,837,000	1,189,000	621,000	431,000
225^2	7,377,000	3,871,000	1,623,000	849,000	590,000
321^2	10,267,000	5,394,000	2,312,000	1,209,000	824,000

Table 8
The Rayleigh-number dependence of the number of iterations to achieve steady state. Ma = 0.01 and Pr = 0.71.

N^2	Ra = 10^3	Ra = 10^4	Ra = 10^5	Ra = 10^6
41^2	153,000	344,000	712,000	1,489,000
57^2	204,000	461,000	985,000	2,061,000
81^2	277,000	629,000	1,341,000	2,859,000
113^2	370,000	845,000	1,863,000	3,891,000
161^2	502,000	1,149,000	2,528,000	5,412,000
225^2	668,000	1,550,000	3,522,000	7,377,000
321^2	915,000	2,116,000	4,796,000	10,267,000

3.8. Benchmark solutions

We now compare our results for the square cavity with differentially heated vertical walls in 2D with existing data. The results of de Vahl Davis [39] were obtained by using the finite-difference method with uniform meshes of rather modest sizes up to 81^2. The local results of de Vahl Davis [39] were fitted with polynomials and extrapolated asymptotically thus they still remain to be among the most comprehensive and accurate benchmark results. The results of Hortmann et al. [42] were obtained by using the finite-volume method accelerated with multi-grid method on non-uniform meshes up to the size of 640^2, and grid-independent results were obtained by extrapolations. Mayne et al. [41] used *h*-adaptive finite-element method which relies on error-estimation to refine mesh adaptively and very fine mesh was used near boundaries. Le Quéré and de Roquefort [44] and Le Quéré [45] used the Chebyshev pseudo-spectral method up to 128^2 spectral resolution, which also yields very accurate results.

In Table 9, we compile our results of the Nusselt numbers, which are extracted from Table 2 unless otherwise stated, and existing data obtained by using finite difference (FD) [39,40], finite-element (FE) [41], finite-volume (FV) [42], and pseudo-spectral (PS) [44,45] methods. In Table 9, our results of the Nusselt numbers are the asymptotic values fixed with the third-order polynomial of Eq. (39). We also include in Table 9 some recent results obtained by using the LB method. Guo et al. [13] used the LBGK model with double-distributions and a relatively coarse mesh of size 128^2. Mezrhab et al. [51] used the hybrid MRT-LBE [8,15], which solves the temperature equation with finite-difference technique, and a fine mesh of size 411^2.

As shown in Table 9, our results of average Nusselt numbers, *i.e.*, $\langle \mathrm{Nu} \rangle$, $\langle \mathrm{Nu} \rangle_0$, and $\langle \mathrm{Nu} \rangle_{1/2}$, agree with the best existing data to at least three significant digits. Our results of local Nusselt numbers, *i.e.*, $\mathrm{Nu}_{\max}$ and $\mathrm{Nu}_{\min}$, as well as their positions, agree with the most accurate results to at least two or three significant figures. Our results are also consistent with the previous results obtained by using the LB methods [13,51].

In Table 10 we compile the results of the local values of hydrodynamic variables including $|\psi_{\mathrm{mid}}|$, $|\psi|_{\max}$, $u_{\max}$, and $v_{\max}$, as well as their positions. For the hydrodynamic variables, our results agree with the best existing data at least three significant figures. As for the positions, our results agree with the existing data to at least two significant figures.

The data in Tables 9 and 10 show that, with a reasonable resolution, our results agree very well with the most accurate data and the MRT-TLBE can yield very accurate benchmark quality results.

4. Rayleigh–Bénard convection in a rectangular cavity heated from below

4.1. Flow configuration and parameters

The flow domain is a rectangle of an aspect ratio $L/H = 2$, *i.e.*, $(x, y) \in [0, 2] \times [0, 1]$, as illustrated in Fig. 4. The temperatures at the bottom and top walls are $\theta = +0.5$ and $\theta = -0.5$, respectively, thus $\Delta\theta = 1$. The left and right vertical walls are stress free. The boundary conditions (bounce-back for $\{f_i\}$ and "anti-bounce-back" for $\{g_i\}$) are applied for the top and bottom horizontal walls, while periodic boundary conditions are applied in the *x* direction. The parameters for the convective flow are: Ra = $2 \cdot 10^3$, 10^4, and $5 \cdot 10^4$; Pr = 0.71 and 7.0. We will also investigate the effects of the Mach number Ma and the boundary conditions for the vertical side walls.

Table 9
Benchmark solutions of the Nusselt numbers.

Ra	Method	⟨Nu⟩	$\langle \mathrm{Nu}\rangle_0$	$\langle \mathrm{Nu}\rangle_{1/2}$	$\mathrm{Nu}_{\max}$	y	$\mathrm{Nu}_{\min}$
10^3	Present	1.1178	1.1178	1.1178	1.5063	0.08843	0.6912
	PS [44]	–	1.1178	1.1178	1.506	0.088	0.691
	FD [40]	–	1.1178	–	1.5064	–	0.6912
	FD [39]	1.118	1.117	1.118	1.505	0.092	0.692
	FE [41]	–	1.1149	–	1.5062	0.08956	0.6913
	LB [13]	–	1.1168	–	1.5004	0.09375	–
10^4	Present	2.2448	2.2448	2.2448	3.5310	0.1443	0.5849
	PS [44]	–	2.245	2.245	3.531	0.144	0.585
	FD [40]	–	2.2449	–	3.5313	–	0.5850
	FD [39]	2.243	2.238	2.243	3.528	0.143	0.586
	FE [41]	–	2.2593	–	3.5305	0.1426	0.5850
	FV [42]	2.24475	–	–	3.53087	0.14601	–
	LB [13]	–	2.2477	–	3.5715	0.1406	–
10^5	Present	4.5216	4.5214	4.5216	7.7161	0.08238	0.7279
	PS [44]	–	4.522	4.523	7.720	0.082	0.728
	FD [40]	–	4.5214	–	7.7216	–	0.7280
	FD [39]	4.519	4.509	4.519	7.717	0.081	0.729
	FE [41]	–	4.4832	–	7.7084	0.08353	0.7282
	FV [42]	4.52164	–	–	7.72013	0.08233	–
	LB [13]	–	4.5345	–	7.7951	0.0781	–
	LB [51]	4.521	–	–	–	–	–
10^6	Present	8.8253	8.8192	8.8254	17.5274	0.03952	0.9769
	PS [45]	8.8252	–	8.8244	17.5343	0.039	0.97948
	SE [47]	8.825	8.824	8.825	17.539	0.039	0.9796
	FD [40]	8.8091	–	–	17.4752	–	0.9798
	FD [39]	8.800	8.817	8.799	17.925	0.0378	0.989
	FE [41]	–	8.8811	–	17.5308	0.03768	0.9845
	FV [42]	8.82513	–	–	17.536	0.03902	–
	LB [13]	–	8.7775	–	17.4836	0.0312	–
	LB [51]	8.824	–	–	–	–	–

Table 10
Benchmark solutions of the hydrodynamic variables.

Ra	Method	$\lvert\psi_{\mathrm{mid}}\rvert$	$\lvert\psi\rvert_{\max}$	(x, y)	$u_{\max}$	y	$v_{\max}$	x
10^3	Present	1.1746	–	–	3.6494	0.8132	3.6974	0.1783
	PS [44]	1.1746	–	–	3.6494	0.813	3.6974	0.178
	FD [39]	1.174	–	–	3.649	0.813	3.697	0.178
	FE [41]	–	–	–	3.6493	0.8125	3.6962	0.1790
	LB [13]	–	–	–	3.6554	0.8125	3.6985	0.1797
10^4	Present	5.0737	–	–	16.1833	0.8232	19.6282	0.1189
	PS [44]	5.0736	–	–	16.183	0.823	19.629	0.119
	FD [39]	5.071	–	–	16.178	0.823	19.617	0.119
	FV [42]	–	–	–	16.1802	0.82551	19.6295	0.12009
	LB [13]	–	–	–	16.0761	0.8203	19.6368	0.1172
10^5	Present	9.1157	9.6179	(0.2843, 0.6015)	34.7424	0.8546	68.6358	0.06586
	PS [44]	9.119	9.619	(0.285, 0.601)	34.75	0.855	68.64	0.066
	FD [39]	9.111	9.612	(0.285, 0.601)	34.73	0.855	68.59	0.066
	FV [42]	–	–	–	34.7399	0.85535	68.6396	0.06719
	LB [13]	–	–	–	34.8343	0.8594	68.2671	0.0625
	LB [51]	–	–	–	34.74	–	68.73	–
10^6	Present	16.3868	16.8149	(0.1503, 0.5468)	64.8336	0.8499	220.5658	0.03776
	PS [45]	16.386	16.811	(0.150, 0.547)	64.83	0.850	220.6	0.038
	FD [39]	16.32	16.750	(0.151, 0.547)	64.63	0.850	219.36	0.0379
	FV [42]	–	–	–	64.8367	0.85036	220.461	0.03887
	LB [13]	–	–	–	65.3606	0.8516	216.415	0.0391
	LB [51]	–	–	–	64.86	–	220.3	–

The volume average Nusselt number ⟨Nu⟩ is defined as follows

$$\langle \mathrm{Nu}\rangle = 1 + \frac{\langle v\theta\rangle H}{\kappa\,\Delta\theta}. \tag{41}$$

The heat flux in the vertical direction is

$$q_y = v\theta - \partial_y\theta. \tag{42}$$

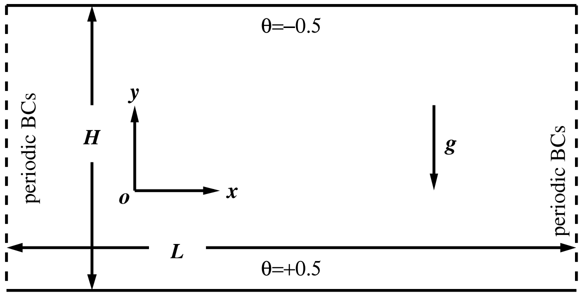

Fig. 4. Illustration of the flow domain for the Rayleigh–Bénard convection in the rectangle ($L = 2H$) heated from below.

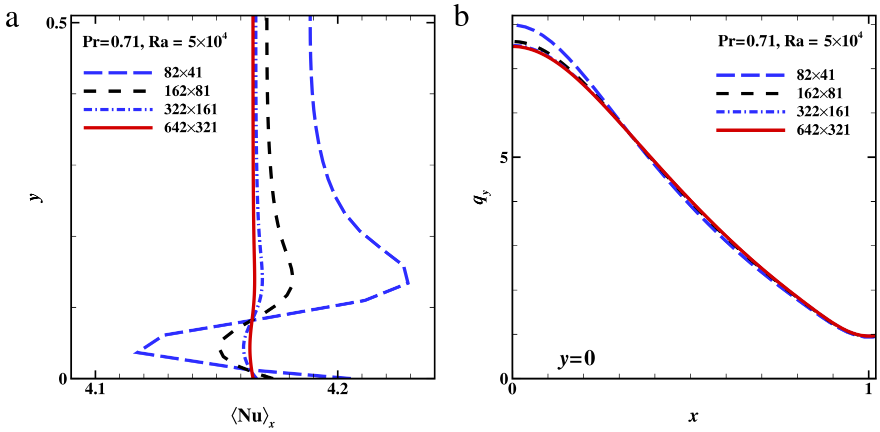

Fig. 5. The Rayleigh–Bénard convection with $\mathrm{Ra} = 5 \cdot 10^4$, $\mathrm{Pr} = 0.71$ and $\mathrm{Ma} = 0.01$. (a) Distribution of the Nusselt number $\langle \mathrm{Nu} \rangle_x$ averaged over x as a function of y. $\langle \mathrm{Nu} \rangle_x$ is symmetric about $y = 1/2$. (b) Distribution of the heat flux $q_y(x)$ at the hot bottom wall $x = 0$.

We compute the volume average Nusselt number $\langle \mathrm{Nu} \rangle$, the Nusselt number at the bottom boundary, Nu_0, and the Nusselt number $\mathrm{Nu}_{1/2}$ at the horizontal center line $y = 1/2$, and the maximum and minimum Nusselt numbers, $\mathrm{Nu}_{\max}$ and $\mathrm{Nu}_{\min}$, at the bottom. We also compute some hydrodynamic quantities in the flow including the maximum value of the stream-function, $|\psi|_{\max}$, the maximum horizontal velocity $u_{\max}$ at $x = 1/2$ and its position, and the maximum vertical velocity $v_{\max}$ at $y = 1/2$. In addition, we compute the critical Rayleigh number Ra_c.

4.2. Grid convergence of flow fields

We use the following mesh sizes to study the convergence behavior of the Rayleigh–Bénard convection flow: 82×41, 162×81, 322×161, and 642×321. The solution with the largest mesh size of 642×321 is used as the reference solution to compute errors in flow fields. The flow fields on the finest mesh (642×321) are interpolated to the grid points of a coarser mesh with a second-order interpolation in two dimensions to compute errors in the flow fields.

Table 11 compiles the errors of flow fields $\boldsymbol{u}$, p, and θ with L_2-norm, for $\mathrm{Pr} = 0.71$ and 7.0. The Mach number is fixed at 0.01. The data in Table 11 show that the convergence rates n for all flow fields are 2.0, indicating that the MRT-TLBE scheme is second-order accurate for all flow fields. If the flow fields are not interpolated to the same grid points, the rates of convergence for all flow fields are about 1.4, similar to the previous case.

4.3. Convergence of the Nusselt numbers

In Fig. 5 we show the convergence behaviors of the Nusselt number averaged over horizontal grid lines, $\langle \mathrm{Nu} \rangle_x$, and the heat flux q_y at the hot bottom wall for the case of $\mathrm{Ra} = 5 \cdot 10^4$ and $\mathrm{Pr} = 0.71$. We use a second-order polynomial to fit the temperature θ along each vertical grid line, which is used in turn to compute its derivative $\partial_y \theta$ in q_y. We observe that with coarse mesh sizes, $\langle \mathrm{Nu} \rangle_x$ oscillates near the boundary $y = 0$. The heat flux at the hot bottom wall seems to converge to grid-size independent results quicker than $\langle \mathrm{Nu} \rangle_x$.

Table 12 compiles the results concerning the convergence behaviors of Nusselt numbers depending on Ra and Pr, with a fixed $\mathrm{Ma} = 0.01$. The average Nusselt numbers, $\langle \mathrm{Nu} \rangle$, Nu_0, and $\mathrm{Nu}_{1/2}$, agree with each other for at least two significant digits even in the case of the smallest mesh size 82×41, and in most cases they agree with each other for three or more significant digits. Note that, without interpolations, the value of $\mathrm{Nu}_{\max}$ is always located at the first fluid node at the bottom

Table 11
Convergence of flow fields $\boldsymbol{u}$, p, and θ with L_2-norm. Ma = 0.01.

Ra		$2 \cdot 10^3$	10^4	$5 \cdot 10^4$
Pr	$N_x \times N_y$	$\|\delta \boldsymbol{u}\|_2$		
0.71	82×41	$1.8235123 \cdot 10^{-3}$	$1.6662503 \cdot 10^{-3}$	$2.4985370 \cdot 10^{-3}$
	162×81	$4.5477030 \cdot 10^{-4}$	$4.1009633 \cdot 10^{-4}$	$6.0755183 \cdot 10^{-4}$
	322×161	$9.3105636 \cdot 10^{-5}$	$8.3432755 \cdot 10^{-5}$	$1.2313076 \cdot 10^{-4}$
	n	2.1750164	2.1892687	2.2009012
		$\|\delta p\|_2$		
	82×41	$7.8884782 \cdot 10^{-4}$	$1.6097741 \cdot 10^{-3}$	$3.1967885 \cdot 10^{-3}$
	162×81	$1.9080679 \cdot 10^{-4}$	$3.9130467 \cdot 10^{-4}$	$7.7196536 \cdot 10^{-4}$
	322×161	$3.8460740 \cdot 10^{-5}$	$7.9254493 \cdot 10^{-5}$	$1.5638540 \cdot 10^{-4}$
	n	2.2087398	2.2016116	2.2062784
		$\|\delta \theta\|_2$		
	82×41	$7.0435664 \cdot 10^{-4}$	$2.0207005 \cdot 10^{-3}$	$5.4430297 \cdot 10^{-3}$
	162×81	$1.7118507 \cdot 10^{-4}$	$4.7893200 \cdot 10^{-4}$	$1.2717761 \cdot 10^{-3}$
	322×161	$3.4601087 \cdot 10^{-5}$	$9.5578827 \cdot 10^{-5}$	$2.5148566 \cdot 10^{-4}$
	n	2.2032327	2.2308896	2.2480329
7.0		$\|\delta \boldsymbol{u}\|_2$		
	82×41	$1.9122279 \cdot 10^{-3}$	$1.9493835 \cdot 10^{-3}$	$3.4416128 \cdot 10^{-3}$
	162×81	$4.7629506 \cdot 10^{-4}$	$4.7715646 \cdot 10^{-4}$	$8.3752414 \cdot 10^{-4}$
	322×161	$9.7572924 \cdot 10^{-5}$	$9.6257877 \cdot 10^{-5}$	$1.6955373 \cdot 10^{-4}$
	n	2.1754817	2.1994687	2.2011312
		$\|\delta p\|_2$		
	82×41	$6.8784479 \cdot 10^{-4}$	$1.3773027 \cdot 10^{-3}$	$3.4770364 \cdot 10^{-3}$
	162×81	$1.6637820 \cdot 10^{-4}$	$3.3417353 \cdot 10^{-4}$	$8.4000603 \cdot 10^{-4}$
	322×161	$3.3555042 \cdot 10^{-5}$	$6.7236855 \cdot 10^{-5}$	$1.6946493 \cdot 10^{-4}$
	n	2.2083303	2.2078132	2.2089964
		$\|\delta \theta\|_2$		
	82×41	$7.3461000 \cdot 10^{-4}$	$2.0946577 \cdot 10^{-3}$	$5.1380574 \cdot 10^{-3}$
	162×81	$1.7842903 \cdot 10^{-4}$	$4.9466298 \cdot 10^{-4}$	$1.1923695 \cdot 10^{-3}$
	322×161	$3.6105038 \cdot 10^{-5}$	$9.8327861 \cdot 10^{-5}$	$2.3523463 \cdot 10^{-4}$
	n	2.2028709	2.2364387	2.2547114

boundary, *i.e.*, $(i, j) = (1, 1/2)$, where $j = 1/2$ means $\delta x/2$ beyond the last fluid node at $j = 1$ while $\mathrm{Nu}_{\min}$ is always located at the mesh center, *i.e.*, $(i, j) = (N_x/2, 1/2)$. As mesh size $N_x \times N_y$ goes to infinity, the locations of $\mathrm{Nu}_{\max}$ and $\mathrm{Nu}_{\min}$ will go to $(x, y) = (0, 0)$ and $(x, y) = (1, 0)$, respectively. Except for the case of $\mathrm{Nu}_{\min}$, the rate of convergence n is about 2.0. It should be noted that for both $\mathrm{Nu}_{\max}$ and $\mathrm{Nu}_{\min}$, the norm is L_∞ which is the most stringent.

Table 13 compiles the results concerning the convergence behaviors of the hydrodynamic quantities under study, depending on Ra and Pr, with Ma = 0.01. These hydrodynamic quantities include the maximum of the absolute value of the stream function, $|\psi|_{\max}$, which is always located at $(x, y) = (1/2, 1/2)$, the maximum x-velocity at the vertical line $x = 1/2$, and the maximum y-velocity at the horizontal center line $y = 1/2$, which is always located at the center of the line $x = 1$. In all cases, the results have agreement of at least two significant digits with the smallest mesh size of 82×41, indicating that mesh-size independent results have been obtained. Overall the results show the MRT-TLBE scheme is of second-order convergence.

The asymptotic values of the Nusselt numbers in Table 12 and those hydrodynamic quantities in Table 13 are obtained by using the least-square fit to the third-order polynomial of Eq. (39). We should mention that in some cases the data obtained with the coarsest mesh of 82×41 are excluded in the least-square fitting. These cases for which the data are excluded from the fitting are marked with "$*$" in both tables.

Table 14 shows the convergence behavior of the average Nusselt number $\langle \mathrm{Nu} \rangle$ depending on the Mach number Ma. The data clearly show that the Mach number has no effect at all on the Nusselt number $\langle \mathrm{Nu} \rangle$. This observation indicates that the Mach number is equivalent to the CFL number for the incompressible TLBE with Boussinesq approximation, thus varying Ma amounts to changing the time-step size, which has no effect on the accuracy of the steady flows studied in this work.

4.4. Flow fields

Fig. 6 illustrates the streamlines, isotherms, and pressure contours for the Rayleigh–Bénard convection with Pr = 0.71, and Ra $= 2 \cdot 10^3$, 10^4, and $5 \cdot 10^4$. When the Rayleigh number is below the critical value of $\mathrm{Ra}_c \approx 1707.762$ [52], the temperature has no horizontal gradient—the only heat transfer mechanism is thermal conduction. Consequently the isotherms are straight horizontal lines. The values of Ra we use are all greater than the critical value $\mathrm{Ra}_c \approx 1707.762$, thus convection takes place as a heat transfer mechanism in addition to conduction. The convective motion due to two counter-rotating vortexes can be clearly seen in the flow patterns shown in Fig. 6. The horizontal temperature gradient

Table 12
Convergence behaviors of Nusselt numbers. Ma = 0.01.The data marked with "∗" are excluded from the least-square fitting to obtain asymptotic values.

Pr	Ra	$N_x \times N_y$	$\langle \mathrm{Nu} \rangle$	Nu_0	$\mathrm{Nu}_{1/2}$	Nu_{max}	Nu_{min}
0.71	$2 \cdot 10^3$	82 × 41	1.2113916	1.2115122	1.2131327	1.7762356	0.62197443
		162 × 81	1.2107538	1.2107701	1.2111999	1.7721196	0.62278374
		322 × 161	1.2105862	1.2105883	1.2106991	1.7711165	0.62296531
		642 × 321	1.2105431	1.2105434	1.2105715	1.7708707	0.62300764
		∞	1.2105286	1.2105285	1.2105286	1.7707886	0.62302137
		n	1.9850927	2.0358459	1.9950204	2.0389039	2.1056930
	10^4	82 × 41	2.6621453	2.6646292	2.6644154	4.4128023	0.79251933*
		162 × 81	2.6569340	2.6572746	2.6575124	4.3536217	0.79270573
		322 × 161	2.6555886	2.6556329	2.6557349	4.3395338	0.79258856
		642 × 321	2.6552461	2.6552517	2.6552830	4.3361637	0.79253953
		∞	2.6551312	2.6551282	2.6551316	4.3350273	0.79251930
		n	1.9979442	2.1098972	1.9998832	2.0544574	1.6131396
	$5 \cdot 10^4$	82 × 41	4.1890216	4.2054264	4.1886300	7.9635650	0.96295756*
		162 × 81	4.1708705	4.1732783	4.1707507	7.6086004	0.96283936
		322 × 161	4.1662151	4.1665341	4.1661836	7.5225797	0.96250197
		642 × 321	4.1650342	4.1650752	4.1650262	7.5024015	0.96238446
		∞	4.1646388	4.1645918	4.1646398	7.4952083	0.96233878
		n	2.0026672	2.1581222	2.0058891	2.0332152	1.7386379
7.0	$2 \cdot 10^3$	82 × 41	1.2138056	1.2139259	1.2155964	1.7637933	0.61674958
		162 × 81	1.2131324	1.2131487	1.2135912	1.7600144	0.61782582
		322 × 161	1.2129558	1.2129578	1.2130719	1.7590917	0.61807162
		642 × 321	1.2129103	1.2129105	1.2129397	1.7588648	0.61812938
		∞	1.2128951	1.2128949	1.2128952	1.7587893	0.61814835
		n	1.9866559	2.0349335	1.9954716	2.0381289	2.0898421
	10^4	82 × 41	2.6170260	2.6189246	2.6197594	3.9213957	0.84034065
		162 × 81	2.6115803	2.6118381	2.6122784	3.8847917	0.84648953
		322 × 161	2.6101782	2.6102127	2.6103540	3.8760752	0.84773176
		642 × 321	2.6098247	2.6098272	2.6098706	3.8739729	0.84799025
		∞	2.6097046	2.6097018	2.6097055	3.8732735	0.84807592
		n	1.9979049	2.0880535	1.9977474	2.0562383	2.1916472
	$5 \cdot 10^4$	82 × 41	3.8836213	3.8928928	3.8825115	6.4560756	1.0908378
		162 × 81	3.8652480	3.8665374	3.8649553	6.2703465	1.1260297
		322 × 161	3.8605636	3.8607326	3.8604890	6.2267504	1.1337171
		642 × 321	3.8593770	3.8593986	3.8593582	6.2164291	1.1353876
		∞	3.8589814	3.8589675	3.8589819	6.2129528	1.1359736
		n	2.0074310	2.1210690	2.0091889	2.0650939	2.1156290

increases with Ra, as indicated by the increasing steepness of the isotherms around the vertical centerline of the rectangle, $x = 1$. When $\mathrm{Ra} = 5 \cdot 10^4$, the isotherms near $x = 1$ are almost vertical, indicating that the convection is the dominant heat transfer mechanism. Also, as Ra increases, the streamlines become more and more asymmetric with respect to the horizontal centerline $y = 1/2$. In Fig. 6 we also show the flow fields obtained by using different Mach numbers, which indicates the fact that the Mach number has little effect on the flow fields.

Fig. 7 shows the flow fields for $\mathrm{Pr} = 7.0$, and $\mathrm{Ra} = 2 \cdot 10^3$, 10^4, and $5 \cdot 10^4$. The viscous effect for $\mathrm{Pr} = 7.0$ is about 10 times of that for $\mathrm{Pr} = 0.71$. Consequently, the convection is considerably weaker when $\mathrm{Pr} = 7.0$. With $\mathrm{Ra} = 2 \cdot 10^3$, the average Nusselt numbers with $\mathrm{Pr} = 7.0$ are slightly larger than their counterparts with $\mathrm{Pr} = 0.71$, while the differences $(\mathrm{Nu}_{max} - \mathrm{Nu}_{min})$ are slightly larger in the case of $\mathrm{Pr} = 0.71$, as shown by the data in Table 12. However, in the cases of $\mathrm{Ra} = 10^4$ and $5 \cdot 10^4$, the Nusselt numbers with $\mathrm{Pr} = 0.71$ not only are larger than their counterparts with $\mathrm{Pr} = 7.0$, but also increase faster with Ra. Nevertheless, the isotherms for both cases of $\mathrm{Pr} = 7.0$ and 0.71 are rather similar to each other qualitatively, although the isotherms with $\mathrm{Pr} = 0.71$ do show larger curvatures in the case of the largest Rayleigh number $\mathrm{Ra} = 5 \cdot 10^4$. We also observe that as Ra increases, the streamlines in the cases of $\mathrm{Pr} = 7.0$ maintain the symmetry with respect to the horizontal centerline $y = 1/2$ relatively better than the corresponding cases of $\mathrm{Pr} = 0.71$. Also, as Ra increases, the vortexes become more square than circular, and the streamlines are more conformed to two square boxes defined by the boundaries of flow domain and the vertical centerline $x = 1$.

The temperature fields for $\mathrm{Pr} = 0.71$ and 7.0 with equal Rayleigh number Ra, as shown in Figs. 6 and 7, respectively, do not exhibit a significant difference. This is further illustrated in Fig. 8 which compares the temperatures for $\mathrm{Ra} = 10^4$ and $\mathrm{Pr} = 0.71$ and 7.0 at two different horizontal lines $y = 1/4$ and $3/4$. Clearly, in most places the magnitude of the temperature for $\mathrm{Pr} = 0.71$ is larger than that for $\mathrm{Pr} = 7.0$, but not significantly. Overall, the temperature for $\mathrm{Pr} = 7.0$ is slightly flatter than that for $\mathrm{Pr} = 0.71$.

Fig. 9 shows the contours of the vertical (y) velocity $v(x, y)$ for $\mathrm{Ra} = 10^4$ and $\mathrm{Pr} = 0.71$ and 7.0. Clearly, the $v(x, y)$ for $\mathrm{Pr} = 7.0$ is more symmetric with respect to the horizontal centerline $y = 1/2$ than that for $\mathrm{Pr} = 0.71$. The contours of $v(x, y) = 0$ for $\mathrm{Pr} = 0.71$ converge from the bottom to the top, while those for $\mathrm{Pr} = 7.0$ diverge only slightly.

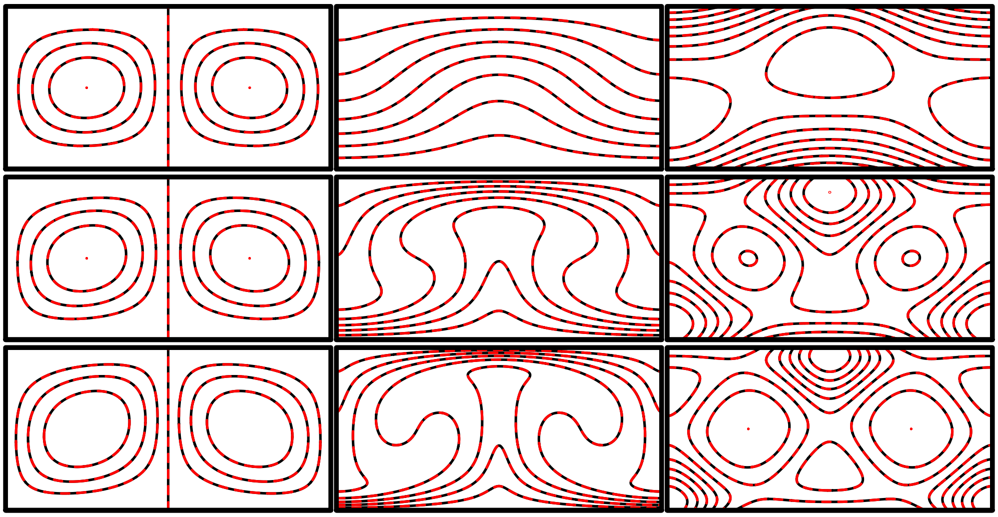

Fig. 6. Contours of flow fields of the Rayleigh–Bénard convection in the rectangle. Pr $= 0.71$. From left to right: the stream-function, the isotherms, and the pressure. From top to bottom: Ra $= 2 \cdot 10^3$, 10^4, and $5 \cdot 10^4$. Solid (black) lines: $N_x \times N_y = 642 \times 321$ and Ma $= 0.01$. Dashed (red) lines: for Ra $= 2 \cdot 10^3$, $N_x \times N_y = 322 \times 161$ and Ma $= 0.05$; and for Ra $= 10^4$ and $5 \cdot 10^4$, $N_x \times N_y = 642 \times 321$, and Ma $= 0.05$ and 0.1, respectively. (For interpretation of the references to colour in this figure legend, the reader is referred to the web version of this article.)

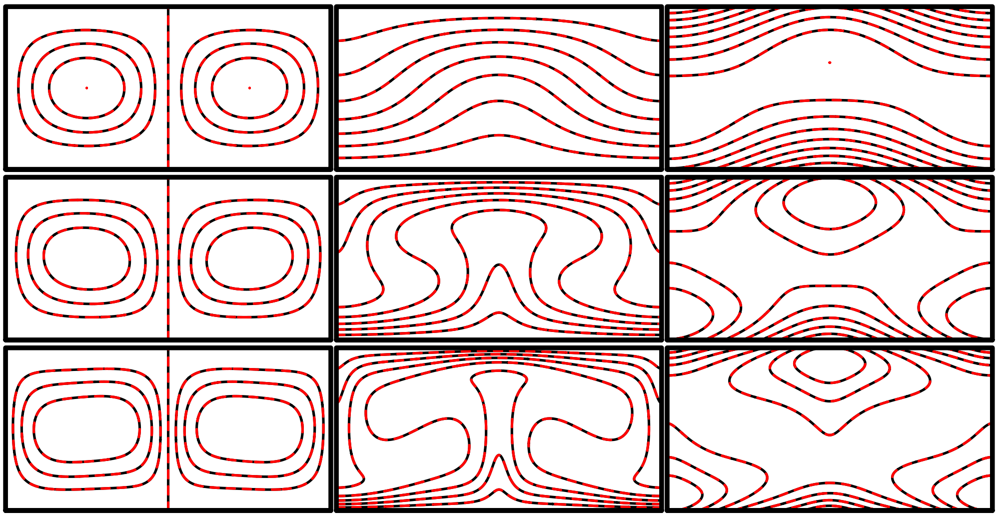

Fig. 7. Similar to Fig. 6. Pr $= 7.0$ and $N_x \times N_y = 642 \times 321$. Solid (black) lines: Ma $= 0.01$. Dashed (red) lines: for Ra $= 2 \cdot 10^3$, Ma $= 0.05$; and for Ra $= 10^4$ and $5 \cdot 10^4$, Ma $= 0.1$. (For interpretation of the references to colour in this figure legend, the reader is referred to the web version of this article.)

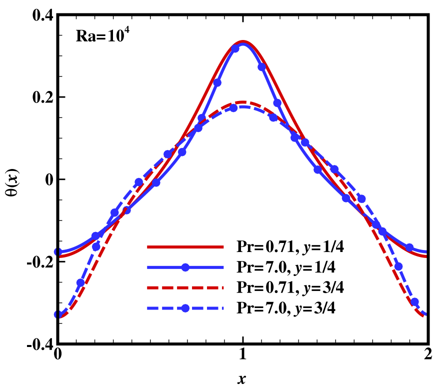

Fig. 8. $\theta(x, y)$ at two horizontal lines $y = 1/4$ and $3/4$. Ra $= 10^4$.

Table 13
Convergence behaviors of hydrodynamic variables. Ma = 0.01. The data marked with "∗" are excluded from the least-square fitting to obtain asymptotic values.

Pr	Ra	$N_x \times N_y$	$\lvert\psi\rvert_{max}$	u_{max}	y	v_{max}
0.71	$2 \cdot 10^3$	82 × 41	1.5645398∗	4.8255910	0.20699909	4.9130905
		162 × 81	1.5643061	4.8212220	0.20701752	4.9058434
		322 × 161	1.5642185	4.8200616	0.20702374	4.9039308
		642 × 321	1.5641924	4.8197615	0.20702504	4.9034388
		∞	1.5641829	4.8196603	0.20702578	4.9032726
		n	1.8605040	1.9784776	1.7726971	1.9821850
	10^4	82 × 41	9.0975682∗	29.185548∗	0.17607948∗	30.630719
		162 × 81	9.0976171	29.163358	0.17603327	30.608401
		322 × 161	9.0975174	29.157681	0.17602864	30.602512
		642 × 321	9.0974752	29.156237	0.17602823	30.601000
		∞	9.0974577	29.155754	0.17602759	30.600488
		n	1.6053941	2.0021411	1.5778553	1.9818841
	$5 \cdot 10^4$	82 × 41	23.385572	83.727706	0.13425853	88.734612
		162 × 81	23.378048	83.606805	0.13401480	88.816569
		322 × 161	23.375886	83.575881	0.13397970	88.838675
		642 × 321	23.375285	83.568009	0.13397128	88.844345
		∞	23.375091	83.565397	0.13397089	88.846228
		n	1.9351737	2.0059524	3.1176058	1.9481354
7.0	$2 \cdot 10^3$	82 × 41	1.5744575	4.8509071	0.20816094	4.9776755
		162 × 81	1.5740952	4.8461445	0.20818166	4.9699493
		322 × 161	1.5739747	4.8448840	0.20818824	4.9679132
		642 × 321	1.5739400	4.8445576	0.20818966	4.9673891
		∞	1.5739280	4.8444482	0.20819041	4.9672126
		n	1.8418261	1.9815514	1.8129577	1.9836670
	10^4	82 × 41	8.9356742	27.805819	0.19771741	34.217912
		162 × 81	8.9323398	27.776768	0.19774395	34.186997
		322 × 161	8.9313824	27.769307	0.19775255	34.178852
		642 × 321	8.9311334	27.767434	0.19775580	34.176790
		∞	8.9310434	27.766794	0.19775646	34.176076
		n	1.9188748	1.9988445	1.9562843	1.9798167
	$5 \cdot 10^4$	82 × 41	21.600066	68.686006∗	0.17721526∗	117.11480
		162 × 81	21.569192	68.547241	0.17721600	117.03686
		322 × 161	21.561009	68.512220	0.17722439	117.01454
		642 × 321	21.558896	68.503380	0.17722749	117.00868
		∞	21.558184	68.500417	0.17722872	117.00660
		n	1.9796398	2.0044751	1.6954514	1.9234752

Table 14
Dependence of convergence behavior of ⟨Nu⟩ on the Mach number Ma. Ra = $5 \cdot 10^4$.

Ma	0.01	0.05	0.10
$N_x \times N_y$	Pr = 0.71		
82 × 41	4.1890216	4.1890216	4.1890216
162 × 81	4.1708704	4.1708704	4.1708704
322 × 161	4.1662151	4.1662151	4.1662151
642 × 321	4.1650342	4.1650342	4.1650342
∞	4.1646387	4.1646387	4.1646387
n	2.0026672	2.0026661	2.0026661
	Pr = 7.0		
82 × 41	3.8836213	3.8836213	3.8836213
162 × 81	3.8652479	3.8652479	3.8652479
322 × 161	3.8605635	3.8605635	3.8605635
642 × 321	3.8593769	3.8593769	3.8593769
∞	3.8589814	3.8589814	3.8589814
n	2.0074310	2.0074324	2.0074324

Fig. 10 shows the vertical velocity $v(x, y)$ at three horizontal lines: $y = 1/4$, $1/2$, and $3/4$. Clearly, the maximum value of $v(x, y)$ for Pr = 0.71 is about one order of magnitude larger than that for Pr = 7.0, as expected.

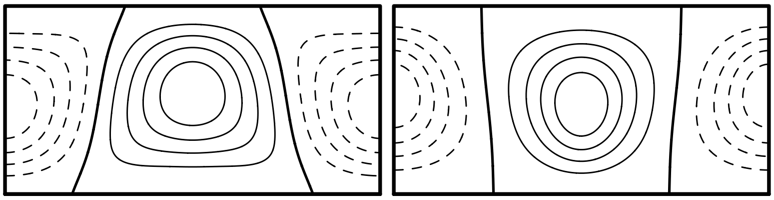

Fig. 9. The contours of the y-velocity $v(x, y)$. Ra $= 10^4$ and $N_x \times N_y = 642 \times 321$. Pr $= 0.71$ (left) and 7.0 (right). Thin solid, dashed, and thick solid lines correspond to positive, negative, and zero values of $v(x, y)$, respectively.

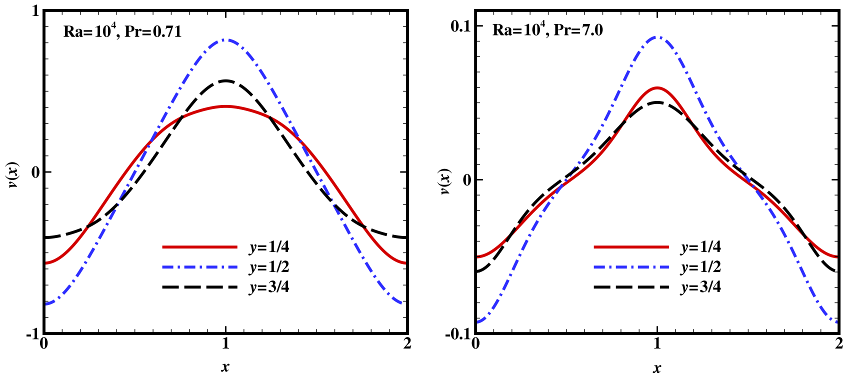

Fig. 10. Vertical (y) velocity $v(x, y)$ at $y = 1/4$, 1/2, and 3/4. Ra $= 10^4$, Pr $= 0.71$ (left) and 7.0 (right).

4.5. *The critical Rayleigh number for the case of* Pr $= 0.71$

We use the MRT-TLBE scheme to determine the critical Rayleigh number Ra_c, beyond which the Rayleigh–Bénard convection occurs. The procedure to determine the onset of the convection is the following. The initial velocity and density fields are quiescent, *i.e.*, $\boldsymbol{u}_0 = \mathbf{0}$ and $\delta\rho_0 = 0$, and the initial temperature is uniform in the x-direction and has a linear profile in the y-direction:

$$\theta(i,j) = \frac{1}{2} - \frac{(2j-1)}{2N_y}, \quad 1 \le i \le N_x,\, 1 \le j \le N_y, \tag{43}$$

so $\theta \in [-0.5, +0.5]$ and it satisfies the boundary conditions. The linear profile of θ is close to its steady state solution when $\mathrm{Ra} < \mathrm{Ra}_c$. We measure the evolution of the maximum y-velocity in the system $v_{\max}(t)$ for a given Ra. The magnitude of $v_{\max}(t)$ will decay if $\mathrm{Ra} < \mathrm{Ra}_c$ and will grow if $\mathrm{Ra} > \mathrm{Ra}_c$. After an initial equilibration, $v_{\max}$ will grow or decay exponentially in a period of time before it is saturated, depending on Ra. We compute the grow rate γ of $v_{\max}(t)$ as a function of Ra. The critical Rayleigh number, Ra_c, is determined by $\gamma(\mathrm{Ra}_c) = 0$ by linearly fitting $\gamma(\mathrm{Ra})$ with the least-square method. Note that the growth rate γ is computed with the dimensionless time $t_n\kappa/N_y^2$.

In Fig. 11 (left) we show the evolution of $v_{\max}(t)$ after the initial equilibration in semi-log scale for Pr $= 0.71$, Ra $= 1685$, 1700, 1715, and 1730, and $N_x \times N_y = 642 \times 321$; we also show the growth rates $\gamma(\mathrm{Ra})$ computed from $v_{\max}(t)$ in Fig. 11 (right). It seems clear that $lg[v_{\max}(t_n)]$ varies linearly in time. We compute the growth rate γ *versus* the rescaled time $t_n\kappa/N_y^2$ as a function of Ra, which also fits a linear function of Ra very well, as shown in Fig. 11 (right).

We compute the critical Rayleigh number Ra_c as a function of the mesh size $N_x \times N_y$ and the results are tabulated in Table 15. The asymptotic value of Ra_c is obtained by using the least-square fit with the third-order polynomial of $h = 1/N_y$ of Eq. (39). For the 2D Rayleigh–Bénard convection considered here, the exact value of Ra_c based on the linear stability theory is about 1707.762 [52]. Our results agree with the exact value of Ra_c for 4 significant digits except for the case of the coarsest mesh size $N_x \times N_y = 22 \times 11$. The asymptotic value of Ra_c differs from its theoretical value by about 0.012%.

4.6. *Effects of boundary conditions*

We use the periodic boundary conditions to represent the stress-free boundary conditions in the lateral direction. Other boundary conditions for the vertical walls are the rigid walls with the adiabatic boundary condition. We will study the effects due to different boundary conditions.

We consider the case of Pr $= 0.71$ and Ra $= 10^4$. The rigid adiabatic lateral walls are represented by the bounce-back boundary conditions for both distributions $\{f_i\}$ and $\{g_i\}$, corresponding to the mass density and the temperature, respectively. The contours of the flow fields are shown in Fig. 12.

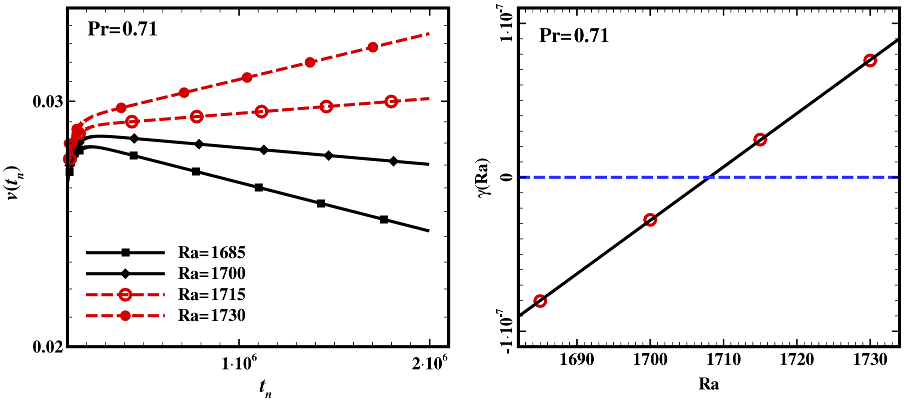

Fig. 11. Determination of the critical Rayleigh number Ra_c. The dependence of the evolution of $v_{\max}(t_n)$ on the Rayleigh number Ra (left) and the corresponding Ra-dependence of the growth rate $\gamma(\mathrm{Ra})$ of $v_{\max}(t_n)$ (right). The symbols are the computed values of γ and the solid straight line is the least-square fit of the computed data. The x-coordinate of the intersection of the solid and dashed lines is the value of Ra_c.

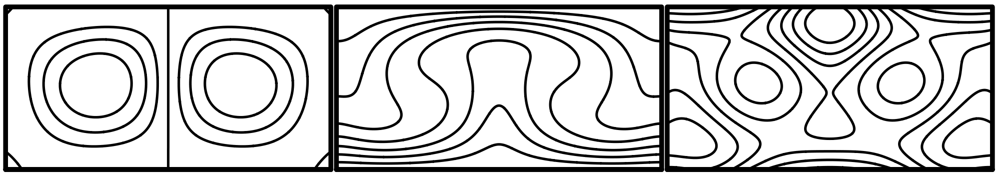

Fig. 12. The Rayleigh–Bénard convection in the 2D rectangle with rigid adiabatic vertical walls. $\mathrm{Pr} = 0.71$, $\mathrm{Ra} = 10^4$, $N_x \times N_y = 642 \times 321$. From left to right: streamlines (left), isotherms (middle), and pressure contours (right).

Table 15
The dependence of the critical Rayleigh number Ra_c on the mesh size $N_x \times N_y$. $\mathrm{Pr} = 0.71$. The asymptotic value of Ra_c is obtained by using the least-square fit with the third-order polynomial of $1/N_y$ of Eq. (39). The data marked with "$*$" are excluded from the least-square fitting to obtain asymptotic values.

$N_x \times N_y$	Ra_c
22×11	$1708.272437 \pm 13.7155^*$
42×21	1707.463181 ± 1.04389
82×41	1707.786862 ± 0.466368
162×81	1707.918852 ± 0.426070
322×161	1707.957846 ± 0.389717
642×321	1707.966558 ± 0.386651
∞	1707.968375 ± 0.379130
n	2.068206673
Theory [52]	1707.762

In contrast with the flow fields with the same Ra and Pr but with the stress-free boundary conditions shown in the middle row of Fig. 6, the flow fields are not affected by the boundary conditions significantly, however, the streamlines do exhibit an observable difference due to different boundary conditions. The streamlines with the rigid adiabatic boundary conditions are more symmetric with respect to the horizontal centerline $y = 1/2$ than the streamlines with the stress-free boundary conditions.

To quantify the effects due to the boundary conditions, we show in Fig. 13 the comparison of temperature profiles $\theta(x)$ at two horizontal lines $y = 1/4$ and $3/4$ with different boundary conditions. The temperature profiles $\theta(x, y)$ at different horizontal lines with the rigid adiabatic vertical walls are similar to those with the stress-free vertical walls, except in the regions near the two lower corners bounded by the rigid adiabatic vertical walls and the hot bottom wall. This is clearly shown in the temperature profile $\theta(x)$ at $y = 1/4$.

We compare the contours of the vertical (y) velocity $v(x, y)$ in Fig. 14. Clearly, the rigid vertical walls force the contours of $v(x, y) = 0$ to be more parallel to the vertical walls thus make the contours of $v(x, y)$ more symmetric with respect to the horizontal centerline $y = 1/2$. The overall effect of the rigid adiabatic walls is flow confinement which inhibits heat convection—the maximum magnitude of the stream-function, $|\psi|_{\max}$, with the stress-free vertical walls is larger than that with the rigid-adiabatic vertical walls and the average Nusselt numbers $\langle \mathrm{Nu} \rangle$ corresponding to the stress-free and the rigid-adiabatic vertical walls are 2.6551 and 2.4049, respectively.

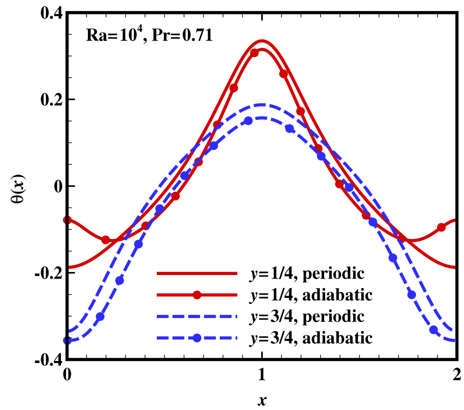

Fig. 13. The effect the boundary conditions on the temperature $\theta(x, y)$ at two horizontal lines $y = 1/4$ and $3/4$ for the Rayleigh–Bénard convection with $\mathrm{Ra} = 10^4$, $\mathrm{Pr} = 0.71$, and $N_x \times N_y = 642 \times 321$.

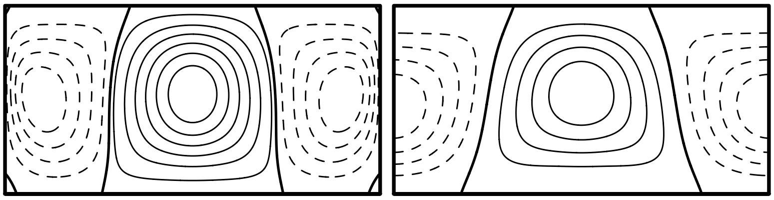

Fig. 14. The effect the boundary conditions on the vertical (y) velocity $v(x, y)$ for the Rayleigh–Bénard convection with $\mathrm{Ra} = 10^4$, $\mathrm{Pr} = 0.71$, and $N_x \times N_y = 642 \times 321$. Left: the rigid adiabatic vertical walls with the bounce-back boundary conditions. Right: the stress-free vertical walls with the periodic boundary conditions.

Table 16
Benchmark solutions of the Nusselt numbers for the Rayleigh–Bénard convection in a 2D rectangle.

Pr	Ra	Method	⟨Nu⟩	Nu_0	$\mathrm{Nu}_{1/2}$	$\mathrm{Nu}_{\max}$,	$\mathrm{Nu}_{\min}$
0.71	$2 \cdot 10^3$	Present	1.2105286	1.2105285	1.2105286	1.7707886	0.62302137
		SP [53]	1.212				
	10^4	Present	2.6551312	2.6551282	2.6551316	4.3350273	0.79251930
		SP [53]	2.661				
	$5 \cdot 10^4$	Present	4.1646388	4.1645918	4.1646398	7.4952083	0.96233878
		SP [53]	4.245				
7.0	$2 \cdot 10^3$	Present	1.2128951	1.2128949	1.2128952	1.7587893	0.61814835
		SP [53]	1.214				
	10^4	Present	2.6097046	2.6097018	2.6097055	3.8732735	0.84807592
		SP [53]	2.618				
	$5 \cdot 10^4$	Present	3.8589814	3.8589675	3.8589819	6.2129528	1.1359736
		SP [53]	3.894				

4.7. Benchmark solutions

Although the Rayleigh–Bénard convection in a 2D rectangle is a well studied case, unlike the previous case of the differentially heated square, there exist scarcely any benchmark results. The only data we could find are the average Nusselt numbers obtained by Clever and Busse by using pseudo-spectral method [53]. We thus compile the results of Clever and Busse [53] and ours in Table 16. Our results in Table 16 are the asymptotic values of the Nusselt numbers given in Table 12.

With the Prandtl number of $\mathrm{Pr} = 0.71$, our result of the average Nusselt number ⟨Nu⟩ agrees with the SP one in three significant digits when $\mathrm{Ra} = 2 \cdot 10^3$, and the relative difference is about 0.12%. The relative difference increases to *ca.* 0.22% and 1.9% for $\mathrm{Ra} = 10^4$ and $5 \cdot 10^4$, respectively. With the Prandtl number of $\mathrm{Pr} = 7.0$, the relative differences between the values of ⟨Nu⟩ obtained by the LB and SP methods are 0.091%, 0.32%, and 0.90%, corresponding to $\mathrm{Ra} = 2 \cdot 10^3$, 10^4, and $5 \cdot 10^4$, respectively. The data in Table 16 clearly show that the LB method systematically under-predicts the average Nusselt number ⟨Nu⟩. This is understandable because the LBE is a second-order method and is more dissipative than the SP method.

We tabulate the hydrodynamic quantities in Table 17. Table 17 only has data obtained by using the LB method in the present work because we have not been able to find other data available in the literature. The data in Table 17 are the asymptotic values in Table 13. The data in Table 17 have at least four significant digits accuracy, as clearly shown in Table 13.

Table 17
Benchmark solutions for the hydrodynamics variables.

Pr	Ra	$\|\psi\|_{\max}$	$u_{\max}$	y	$v_{\max}$
0.71	$2\cdot10^3$	1.5641829	4.8196603	0.20702578	4.9032726
	10^4	9.0974577	29.155754	0.17602759	30.600488
	$5\cdot10^4$	23.375091	83.565397	0.13397089	88.846228
7.0	$2\cdot10^3$	1.5739280	4.8444482	0.20819041	4.9672126
	10^4	8.9310434	27.766794	0.19775646	34.176076
	$5\cdot10^4$	21.558184	68.500417	0.17722872	117.00660

5. Conclusions

In this work we employ the lattice Boltzmann equation with multiple-relaxation-time collision model to simulate thermo-hydrodynamics in two dimensions. The MRT-TLBE consists of two sets of distributions: one with nine velocities (D2Q9) for the mass and momentum conservation equations, and other with five velocities (D2Q5) for the advection–diffusion equation for the temperature. This approach is valid under the Boussinesq approximation. The MRT-TLBE model is used to simulate the following two flows. The first is the square cavity with differentially heated vertical walls for Rayleigh number Ra $= 10^3$, 10^4, 10^5 and 10^6, and Prandtl number Pr $= 0.71$. The second case is the Rayleigh–Bénard convection in a rectangle heated from below and under the influence of gravity for Ra $= 2\cdot10^3$, 10^4 and $5\cdot10^4$, and Pr $= 0.71$ and 7.0.

We systematically study the convergence behavior of the MRT-TLBE scheme, the effect of the Mach number, and the effects due to the stress-free and rigid-adiabatic wall boundary conditions. We compute various Nusselt numbers and hydrodynamic quantities and compare them with existing benchmark data. The results show that the MRT-TLBE scheme can yield benchmark quality results.

Our results demonstrate that the MRT-TLBE scheme is second-order accurate for incompressible thermo-hydrodynamic flows with the Boussinesq approximation. We also find that the Mach number, which is equivalent to the CFL number, has little effect on the accuracy of the MRT-TLBE simulations. This significantly differs from the incompressible athermal flows without the advection–diffusion equation for the temperature, for which the error is of second-order in Mach number. The MRT-TLBE scheme is stable so long as the Mach number is kept below a certain critical value, and the larger the Mach number, the larger the effective time step size, hence the more efficient computationally. We note that it is imperative to use the MRT-TLBE scheme so the boundary conditions for the velocity and temperature fields can be accurately realized, which is impossible for the LBGK-type of scheme with a single relaxation time to achieve.

We also investigate the effects of the relaxation rates s_e and s_ε to the MRT-TLBE simulations and find that they have little effect. We thus use the two-relaxation-time (TRT) model, because, unlike the athermal flows, the stability is not severely affected by the acoustic waves in the system.

Acknowledgments

JW and DHW are supported by the State Key Basic Research Development Program (2012CB417204), the National Natural Science Foundation (grant No. 41175064), and the R&D Special Fund for Public Welfare Industry (Meteorology) by the Ministry of Finance and the Ministry of Science and Technology (grant Nos. GYHY200806007 and GYHY201006014). LSL is supported by the National Science Foundation (NSF) of the United States through Grant No. DMS-0807983 and the Richard F. Barry Jr. Endowment at the Old Dominion University.

References

[1] D. Yu, R. Mei, L.-S. Luo, W. Shyy, Viscous flow computations with the method of lattice Boltzmann equation, Prog. Aerospace Sci. 39 (5) (2003) 329–367.
[2] L.-S. Luo, M. Krafczyk, W. Shyy, Lattice Boltzmann method for computational fluid dynamics, in: R. Blockley, W. Shyy (Eds.), Encyclopedia of Aerospace Engineering, Wiley, New York, 2010, pp. 651–660 (Chapter 56).
[3] F. Alexander, S. Chen, J. Sterling, Lattice Boltzmann thermohydrodynamics, Phys. Rev. E 47 (4) (1993) R2249–R2252.
[4] G. McNamara, B. Alder, Analysis of the lattice Boltzmann treatment of hydrodynamics, Physica A 194 (1993) 218–228.
[5] Y. Chen, H. Ohashi, M. Akiyama, Heat-transfer in lattice BGK modeled fluid, J. Stat. Phys. 81 (1–2) (1995) 71–85.
[6] G. McNamara, A. Garcia, B. Alder, Stabilization of thermal lattice Boltzmann models, J. Stat. Phys. 81 (1/2) (1995) 395–408.
[7] G. McNamara, A. Garcia, B. Alder, A hydrodynamically correct thermal lattice Boltzmann model, J. Stat. Phys. 87 (5/6) (1997) 1111–1121.
[8] P. Lallemand, L.-S. Luo, Theory of the lattice Boltzmann method: acoustic and thermal properties in two and three dimensions, Phys. Rev. E 68 (3) (2003) 036706.
[9] J. Eggels, J. Somers, Numerical-simulation of free convective flow using the lattice-Boltzmann scheme, Int. J. Heat Fluid Flow 16 (5) (1995) 357–364.
[10] X. He, L.-S. Luo, A priori derivation of the lattice Boltzmann equation, Phys. Rev. E 55 (6) (1997) R6333–R6336.
[11] X. He, L.-S. Luo, Theory of lattice Boltzmann method: from the Boltzmann equation to the lattice Boltzmann equation, Phys. Rev. E 56 (6) (1997) 6811–6817.
[12] X. He, S. Chen, G. Doolen, A novel thermal model for the lattice Boltzmann method in incompressible limit, J. Comput. Phys. 146 (1) (1998) 282–300.
[13] Z. Guo, B. Shi, C. Zheng, A coupled lattice BGK model for the Boussinesq equations, Int. J. Numer. Meth. Fluids 39 (4) (2002) 325–342.
[14] Z. Guo, C. Zheng, B. Shi, T. Zhao, Thermal lattice Boltzmann equation for low Mach number flows: decoupling model, Phys. Rev. E 75 (2007) 036704.
[15] P. Lallemand, L.-S. Luo, Hybrid finite-difference thermal lattice Boltzmann equation, Int. J. Mod. Phys. B 17 (1/2) (2003) 41–47.

[16] P. Lallemand, L.-S. Luo, Theory of the lattice Boltzmann method: dispersion, dissipation, isotropy, Galilean invariance, and stability, Phys. Rev. E 61 (6) (2000) 6546–6562.
[17] D. d'Humières, I. Ginzburg, M. Krafczyk, P. Lallemand, L.-S. Luo, Multiple-relaxation-time lattice Boltzmann models in three-dimensions, Philos. Trans. R. Soc. Lond. A 360 (1792) (2002) 437–451.
[18] L.-S. Luo, W. Liao, X. Chen, Y. Peng, W. Zhang, Numerics of the lattice Boltzmann method: effects of collision models on the lattice Boltzmann simulations, Phys. Rev. E 83 (5) (2011) 056710.
[19] D. d'Humières, Generalized lattice-Boltzmann equations, in: B.D. Shizgal, D.P. Weave (Eds.), Rarefied Gas Dynamics: Theory and Simulations, in: Prog. Astronaut. Aeronaut., Vol. 159, AIAA, Washington, DC, 1992, pp. 450–458.
[20] I. Ginzburg, Equilibrium-type and link-type lattice Boltzmann models for generic advection and anisotropic-dispersion equation, Adv. Water Res. 28 (11) (2005) 1171–1195.
[21] I. Ginzburg, Generic boundary conditions for lattice Boltzmann models and their application to advection and anisotropic dispersion equations, Adv. Water Res. 28 (11) (2005) 1196–1216.
[22] I. Ginzburg, Variably saturated flow described with the anisotropic lattice Boltzmann methods, Comput. Fluids 35 (8–9) (2006) 831–848.
[23] I. Ginzburg, Lattice Boltzmann modeling with discontinuous collision components: hydrodynamic and advection–diffusion equations, J. Stat. Phys. 126 (1) (2007) 157–206.
[24] I. Ginzburg, D. d'Humières, Lattice Boltzmann and analytical modeling of flow processes in anisotropic and heterogeneous stratified aquifers, Adv. Water Res. 30 (11) (2007) 2202–2234.
[25] I. Ginzbourg, D. d'Humières, Local second-order boundary methods for lattice Boltzmann models, J. Stat. Phys. 84 (5/6) (1996) 927–971.
[26] I. Ginzburg, D. d'Humières, Multireflection boundary conditions for lattice Boltzmann models, Phys. Rev. E 68 (6) (2003) 066614.
[27] D.P. Lockard, L.-S. Luo, S.D. Milder, B.A. Singer, Evaluation of PowerFLOW for aerodynamic applications, J. Stat. Phys. 107 (2002) 423–478.
[28] C. Pan, L.-S. Luo, C. Miller, An evaluation of lattice Boltzmann schemes for porous medium flow simulation, Comput. Fluids 35 (8/9) (2006) 898–909.
[29] P. Dellar, An interpretation and derivation of the lattice Boltzmann method using Strang splitting, Comput. Math. Appl. (2011) published online (http://dx.doi.org/10.1016/j.camwa.2011.08.047).
[30] I. Ginzbourg, P.M. Adler, Boundary flow condition analysis for the three-dimensional lattice Boltzmann model, J. Phys. II 4 (2) (1994) 191–214.
[31] I. Ginzburg, F. Verhaeghe, D. d'Humières, Two-relaxation-time lattice Boltzmann scheme: about parametrization, velocity, pressure and mixed boundary conditions, Commun. Comput. Phys. 3 (2008) 427–478.
[32] I. Ginzburg, F. Verhaeghe, D. d'Humières, Study of simple hydrodynamic solutions with the two-relaxation-times lattice Boltzmann scheme, Commun. Comput. Phys. 3 (3) (2008) 519–581.
[33] I. Ginzburg, D. d'Humières, A. Kuzmin, Optimal stability of advection–diffusion lattice Boltzmann models with two relaxation times for positive/negative equilibrium, J. Stat. Phys. 139 (6) (2010) 1090–1143.
[34] A. Kuzmin, I. Ginzburg, A. Mohamad, The role of the kinetic parameter in the stability of two-relaxation-time advection–diffusion lattice Boltzmann schemes, Comput. Math. Appl. 61 (12) (2011) 3417–3442.
[35] I. Ginzburg, Truncation errors, exact and heuristic stability analysis of two-relaxation-times lattice Boltzmann schemes for anisotropic advection–diffusion equation, Commun. Comput. Phys. 11 (5) (2012) 1439–1502.
[36] L.-S. Luo, Unified theory of the lattice Boltzmann models for nonideal gases, Phys. Rev. Lett. 81 (1998) 1618–1621.
[37] Z. Guo, C. Zheng, B. Shi, Discrete lattice effects on the forcing term in the lattice Boltzmann method, Phys. Rev. E 65 (2002) 046308.
[38] G. de Vahl Davis, I.P. Jones, Natural-convection in a square cavity: a comparison exercise, Int. J. Numer. Meth. Fluids 3 (3) (1983) 227–248.
[39] G. de Vahl Davis, Natural-convection of air in a square cavity: a bench-mark numerical-solution, Int. J. Numer. Meth. Fluids 3 (3) (1983) 249–264.
[40] P.X. Yu, Z.F. Tian, Compact computations based on a stream-function-velocity formulation of two-dimensional steady laminar natural convection in a square cavity, Phys. Rev. E 85 (2012) 036703.
[41] D. Mayne, A.S. Usmani, M. Crapper, *h*-adaptive finite element solution of high Rayleigh number thermally driven cavity problem, Int. J. Numer. Meth. Heat Fluid Flow 10 (5–6) (2000) 598–615.
[42] M. Hortmann, M. Perić, G. Scheuerer, Finite volume multigrid prediction of laminar natural-convection: bench-mark solutions, Int. J. Numer. Meth. Fluids 11 (2) (1990) 189–207.
[43] G. Croce, G. Comini, W. Shyy, Incompressible flow and heat transfer computations using a continuous pressure equation and nonstaggered grids, Numer. Heat Transfer B 38 (3) (2000) 291–307.
[44] P. Le Quéré, T.A. de Roquefort, Computation of natural convection in two-dimensional cavities with Chebyshev polynomials, J. Comput. Phys. 57 (2) (1985) 210–228.
[45] P. Le Quéré, Accurate solutions to the square thermally driven cavity at high Rayleigh number, Comput. Fluids 20 (1) (1991) 29–41.
[46] A.Y. Gelfgat, Implementation of arbitrary inner product in the global Galerkin method for incompressible Navier–Stokes equations, J. Comput. Phys. 211 (2) (2006) 513–530.
[47] T. Giesdal, C.E. Wasberg, B.A.P. Reif, Spectral element benchmark simulations of natural convection in two-dimensional cavities, Int. J. Numer. Meth. Fluids 50 (11) (2006) 1297–1319.
[48] S.L. Hou, Q. Zou, S. Chen, G.D. Doolen, A.C. Cogley, Simulation of cavity flow by the lattice Boltzmann method, J. Comput. Phys. 118 (1995) 329–347.
[49] P.J. Dellar, Bulk and shear viscosities in lattice Boltzmann equations, Phys. Rev. E 64 (3) (2001) 031203.
[50] P. Dellar, Incompressible limits of lattice Boltzmann equations using multiple relaxation times, J. Comput. Phys. 190 (2) (2003) 351–370.
[51] A. Mezrhab, M. Bouzidi, P. Lallemand, Hybrid lattice-Boltzmann finite-difference simulation of convective flows, Comput. Fluids 33 (4) (2004) 623–641.
[52] W.H. Reid, D.L. Harris, Some further results on the Bénard problem, Phys. Fluids 1 (2) (1958) 102–110.
[53] R.M. Clever, F.H. Busse, Transition to time-dependent convection, J. Fluid Mech. 65 (1974) 625–645. (Part 4).